Materials Today Bio 24 (2024) 100929

Contents lists available at ScienceDirect

Materials Today Bio

journal homepage: www.journals.elsevier.com/materials-today-bio

DLP fabrication of HA scaffold with customized porous structures to regulate immune microenvironment and macrophage polarization for enhancing bone regeneration

Shilang Xiong [a,1], Yinuo Zhang [b,1], Jianhua Zeng [c], Jingyu Zhou [d], Shiwei Liu [e], Peng Wei [d], Hantian Liu [d], Feng Yi [d], Zongmiao Wan [a], Long Xiong [d,*], Bin Zhang [a,**], Jingtang Li [f,***]

[a] Department of Orthopedics, First Affiliated Hospital of Nanchang University, No. 17 Yong Wai Zheng Street, Nanchang, Jiangxi, 330006, China
[b] Department of Orthopedics, Huashan Hospital, Fudan University, 12 Middle Wulumuqi Road, Shanghai, 200040, China
[c] Department of Spine Surgery, Shanghai East Hospital, School of Medicine, Tongji University, Shanghai, 200092, China
[d] Department of Orthopedics, Second Affiliated Hospital of Nanchang University, Nanchang, Jiangxi, 330006, China
[e] Department of Orthopedics, Ganzhou People's Hospital No.16, Mei Guan Road, Zhang Gong District, Ganzhou, Jiangxi, 341000, China
[f] Department of Traumatology, Jiangxi Provincial People's Hospital the First Affiliated Hospital of Nanchang Medical College, Nanchang, Jiangxi, 330006, China

ARTICLE INFO

Keywords:
Bone regeneration
Immunological environment
3D printing technology
Digital light projection
Pore size

ABSTRACT

The immune microenvironment plays a pivotal role in osteoanagenesis. Biomaterials can modulate osteogenic efficacy by inducing specific local immune reactions. As 3D-printing technology advances, digital light projection printing has emerged as a promising method for creating large scale, high-precision biomaterial scaffolds. By adjusting the solid content and the sintering conditions during printing, the pore size of biomaterials can be meticulously controlled. Yet, the systematic influence of pore size on the immune microenvironment remains uncharted. We fabricated 3D-printed hydroxyapatite bioceramic scaffolds with three distinct pore sizes: 400 μm, 600 μm, and 800 μm. Our study revealed that scaffolds with a pore size of 600 μm promote macrophage M2 polarization, which is achieved by upregulating interferon−beta and HIF-1α production. When these materials were implanted subcutaneously in rats and within rabbit skulls, we observed that the 600 μm scaffolds notably improved the long-term inflammatory response, fostered vascular proliferation, and augmented new bone growth. This research paves the way for innovative therapeutic strategies for treating large segmental bone defects in clinical settings.

1. Introduction

Immune cells play a vital role in maintaining angiogenesis and regulating bone remodeling after the implantation of bone biomaterial scaffolds. Changes in the immune microenvironment caused by immune cells can lead to host reactions and impaired function, while an appropriate immune response is crucial for tissue repair and bone regeneration [1–3]. Designing bone biomaterial scaffolds with the capability to regulate the immune microenvironment is a strategy to achieve more effective bone regeneration [4,5]. Macrophages are the most critical regulatory and effector cells in the immune microenvironment and have been widely applied to detect the immunomodulatory properties of biomaterials [6,7]. After implantation, biomaterials are first encountered by macrophages, which are among the primary immune cells involved in the interaction with biomaterials. Macrophages possess phagocytic functions, clear necrotic tissue, and secrete a variety of cytokines, chemokines, and growth factors [8,9].

Macrophages exhibit significant functional plasticity, altering their physiological characteristics based on environmental changes and presenting with different functional phenotypes. Broadly, polarized macrophage phenotypes are categorized into M1 (pro-inflammatory), which are not conducive to wound healing and tissue remodeling, and M2 (pro-healing) macrophages [10–14]. M1 macrophages are typically induced by interferon-γ, expressing surface markers CC-chemokine

* Corresponding author.
** Corresponding author. Department of Orthopedics, First Affiliated Hospital of Nanchang University, Nanchang, Jiangxi, 330006, China.
*** Corresponding author.
E-mail addresses: ncxionglong2@126.com (L. Xiong), 609901889@qq.com (B. Zhang), 24226942@qq.com (J. Li).
[1] These authors have contributed equally to this work.

https://doi.org/10.1016/j.mtbio.2023.100929
Received 14 October 2023; Received in revised form 24 November 2023; Accepted 23 December 2023
Available online 29 December 2023

receptor 7 (CCR7) and inducible nitric oxide synthase (iNOS), while M2 macrophages are usually induced by IL-4, expressing surface markers arginase 1 (ARG-1) and CD206 [3,15]. It has been suggested that many parameters of biomaterials, including the composition and surface topography of the scaffold, can affect the macrophage polarization [16–20]. Surface topography is a key parameter of biomaterial scaffolds that can direct the macrophage fate [21].

Pore size, as an important feature of scaffold surface topography, has been demonstrated to have a crucial impact on the infiltration of macrophages, neovascularization, and the host response to in situ tissue regeneration [22]. The pore size and porosity of the scaffold are vital factors in the scaffold's interaction with macrophages and in the stimulation of macrophage polarization towards M1 or M2 phenotypes [21,23]. Furthermore, tailoring the appropriate scaffold porosity and pore size can provide an optimal surface for bone cell attachment and proliferation, offering proper mechanical support and cell-cell interactions to promote bone cell growth and differentiation [24,25]. Generally, in hydroxyapatite (HA) scaffolds, smaller pore sizes (100–400 μm) tend to promote M1 macrophage polarization, favoring cell invasion and angiogenesis [26,27], while larger pore sizes (400–800 μm) are more likely to guide M2 macrophage differentiation [28], benefiting osteoblast attachment and spreading, as well as ensuring adequate nutrient and oxygen delivery. Rather than being a scaffold aimed at minimizing potential harmful host reactions, adjusting the pore size of the scaffold helps regulate M2 macrophages, promoting repair and anti-inflammatory processes around the scaffolds [29].

Various techniques have been devised for creating porous scaffolds with varying pore sizes, such as: separation [30], freeze-drying [31], solvent casting [32], gas foaming [33], and electrospinning [34]. Although the scaffolds produced by these methods have different micron-scale porous structures, the size of each pore is not controllable, which is not conducive to the establishment of a stable immune microenvironment. According to recent studies, utilization of 3D printing technology is a successful strategy in fabricating bioceramic scaffolds with precise porosity for bone repair [35,36]. In addition, the practical application of bone biomaterial scaffolds not only needs a specific porous structure to modulate biological activity, but also requires large-scale dimensions and a tailored shape to match the defect situation [37]. However, obtaining bioceramics with large dimensions is challenging because of the ceramics' high brittleness and shrinkage during the process of printing and sintering. Digital light projection (DLP) based on UV-curable resin is a promising 3D printing technology providing an unparalleled platform for the production of complex porous scaffolds with high resolution and large-scale dimensions [35,38]. DLP technology exhibits distinct benefits in the production of intricate ceramic bodies with a vast scale for clinical use and with optimal accurate porosity to modulate bone immune response [39–41]. However, there is no uniform answer to the appropriate pore size, as it heavily relies on the particular application and the scaffold material composition.

For this study, we fabricated HA scaffolds in three distinct pore sizes: 400 μm, 600 μm, and 800 μm [42]. Macrophages were co-cultured with scaffolds, and differentially expressed genes (DEGs) were detected using RNA-sequencing technology. This enriched the characteristics of the symbiotic niche in terms of biological function, cellular composition, molecular function, and signaling pathways. Ultimately, through histology and DEGs functional enrichment analysis, we comprehensively elucidated the involvement of macrophages in the bone healing mechanism for the three scaffold materials with varying pore sizes printed using DLP technology. It demonstrated the macrophage polarization process, cellular functions, and regulatory roles in signal transduction composed of the implanted scaffold, recruited cells, and newly formed tissues. This suggests potential molecular biological mechanisms for further research and more effective utilization of the immune microenvironment for bone regenerative scaffold materials.

In this study, in vivo and in vitro experiments were conducted simultaneously on HA scaffolds of three sizes: 400 μm, 600 μm, and 800 μm. In an immune microenvironment, macrophages (RAW264.7), bone marrow stromal cells (BMSCs), and human umbilical vein endothelial cells (HUVECs) were cultured in vitro. The polarization of macrophages as well as osteogenic and angiogenic conditions were examined. The osteogenic and angiogenic effects of the scaffolds were confirmed by utilizing a subcutaneous implant model in rat dorsum and a rabbit cranial model. It is anticipated that this research can demonstrate the immunomodulatory role of pore size and contribute to potential applications in bone tissue regeneration scaffolds based on morphological design. Scheme 1 illustrates the entire research procedure.

2. Materials and methods

2.1. DLP printing of scaffolds

The scaffold was printed using an ink containing UV-curable resins and HA. In the printing ink, commercial urethane acrylate (Neorad, Taiwan) and poly (ethylene glycol) diacrylate (PEGDA-400) were employed as photosensitive elements in the ratio of 3:1. To prepare the printing inks, the HA (P100, Baiameng, China) powder with mass fraction of 50 % was ball milled with photosensitive resin, dispersant (BYK-2155; BYK Chemie, Germany), and photoinitiator (diphenyl (2,4,6-trimethylbenzoyl) phosphine oxide; TPO) for 10 hours. Using SolidWorks (Dassault Systemes, France), the chip model was projected, which was then saved as an STL file and prepared with Magics 22 (materialise, Belgium) for the printing process.

The entity was generated by the DLP printer. The thickness of the layer was 50 μm, and the exposure was 800 ms. Finally, the ceramic green body was put into a muffle furnace and sintered at 1150 °C for 2 h. There is no difference among 400 μm, 600 μm and 800 μm scaffold but the pore size.

2.2. Characterization of the scaffolds

Each specimen received a sputter coat of gold for micromorphological observation via scanning electron microscopy (SEM, JSE-5900LV, Japan). To conduct compress tests, the materials that meet the experimental requirements have been prepared with orientations of 0°, 45°, and 90°. At a 1 mm/min cross-head speed, we derived the stress-strain curve (Shimadzu AGS-X-50 N, Japan) for the scaffolds, determining the compressive strength from it. X-ray diffraction was employed to assess the scaffold's phase composition. The scaffold's hydrophilicity was gauged by determining the water contact angle in a drop experiment (Lauda Scientific LSA100, Germany). The diameter of the scaffold is 6 mm and the height is 2 mm.

2.3. Co-culture of scaffolds and macrophages

RAW 264.7 cells (Procell, China) were seeded on 3D-printed porous scaffolds with distinct pore sizes at 1.0×10^5 cells/well in six-well culture plates. Subsequently, the wells were filled with culture medium. After three days of culture, the scaffolds were transferred to new plates. The scaffolds were fixed with a glutaraldehyde solution for an hour. The scaffolds were then dehydrated in gradient alcohol solution concentrations and gold-coated. SEM was employed to examine the cells that had adhered to the scaffolds.

2.4. Transcriptome analysis

Using RNA sequencing (RNA-seq), gene expression in various scaffold macrophages was examined to study the mechanisms and signaling pathways of macrophage polarization on scaffolds with varying pore diameters. The macrophages were placed in a 6-well plate (1.0×10^5 cells/well) and co-cultured with various scaffolds for 3 days. Cells were collected by centrifugation after 3 days, lysed using TRIzol reagent, and

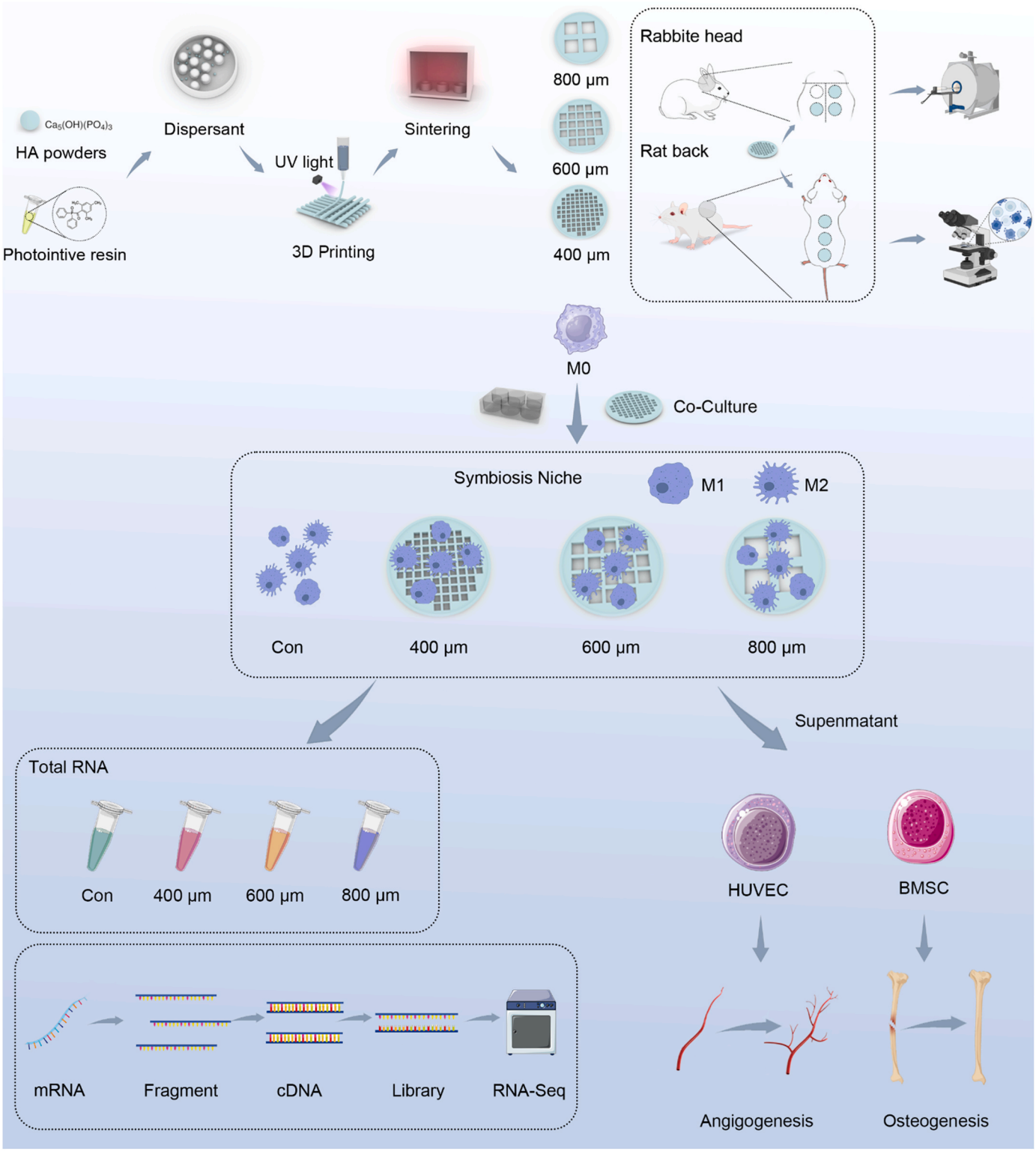

Scheme 1. Schematic diagram of using three distinct scaffolds with varying pore sizes to treat bone defects: In vitro studies have shown that scaffold with 600 μm pores promoted macrophage M2 polarization. The scaffold with 600 μm pores was found to promote vascular regeneration in vivo subcutaneous experiments in rats, and promote new bone formation in rabbit skull defect models. Full transcriptome analysis was performed on the scaffold.

then were quickly frozen. The RNA samples extracted were then sequenced using the Illumina NovaSeq 6000 platform. We applied a logarithmic transformation (base 10) to the gene expression metrics (measured in RPKM). Using the R software, we conducted enrichment assessments for DEGs, GO annotations, and pathways from Kyoto Encyclopedia of Genes and Genomes (KEGG).

2.5. *In vitro experiments*

2.5.1. *Cell culture*

Using 6 well plates, 1.0×10^5 BMSCs and HUVECs (Procell, China) were respectively seeded in each well, which was formulated by mixing the fresh culture medium with the culture medium collected after three

days of macrophage cultivation at a 1:1 ratio. The control group didn't receive any added material.

2.5.2. Western blot analysis

The cells were lysed in RIPA buffer (Servicebio, China) with a protease inhibitor (PMSF, Servicebio, China) using routine procedures to extract total proteins. Lysates were centrifuged at 12,000 rpm for 10 min, followed by the transfer of supernatants to fresh EP tubes. The BCA protein assay was used for protein quantification. Each sample (25 μg) was loaded onto a 12.5 % SDS-PAGE. The membrane was treated with 5 % non-fat milk for 1 h and then washed three times with TBST (Servicebio, China). After washing, membranes were left overnight at 4 °C with anti–IFN–β (1:1000, Abcam, UK) and anti–HIF–1 alpha (1:1000, Abcam, UK) antibodies. After washing, the membranes were incubated for 2 h with anti-rabbit secondary antibodies. Membranes were developed using enhanced chemiluminescence (ECL).

2.5.3. Real-time quantitative PCR

To assess macrophage polarization, we determined the expression levels of polarization differentiation-related genes in RAW 264.7 co-cultured with scaffolds using RT-qPCR. After a 3-day incubation of RAW 264.7, Trizol (Vazyme Biotech Co., Ltd., Nanjing, China) was used for total RNA extraction. The SweScript RT I first strand cDNA synthesis kit was employed to reverse transcribe 500 ng of RNA into complementary DNA (cDNA) (Servicebio, China). The cDNA was then mixed with PCR Master Mix (Servicebio, China). RT-qPCR reactions were conducted for the genes: CCR7, iNOS, ARG-1, and CD206. The relative gene expression was determined utilizing the ΔΔCT approach, with GAPDH serving as the internal reference gene for normalization.

To further assess the influence of different pore-sized scaffolds on the immune environment and its subsequent effects on osteogenesis and angiogenesis, we used a specialized medium mixing the fresh culture medium with the supernatant collected after three days of co-culture of macrophages and scaffolds at a 1:1 ratio for BMSCs and HUVECs. BMSCs and HUVECs were respectively planted in 6-well plates at a concentration of 1.0×10^5 cells/well using mixed culture medium, and the cultivation was continued for three days. In the end, related osteogenic genes like bone morphogenetic protein-2 (BMP-2), collagen 1 (COL1), endothelial nitric-oxide synthase (eNOS), and vascular endothelial growth factor (VEGF) were detected using RT-qPCR. The relative gene expression was determined utilizing the ΔΔCT approach, with GAPDH serving as the internal reference gene for normalization. The sequences of the primers utilized for this research are provided in Table 1.

2.6. In vivo experiments

2.6.1. Angiogenesis in vivo

All experiments adhered to the guiding principles and were approved by the Ethical Committee of Nanchang University, China (approval reference number: No. NCULAE-20221031041 and No. NCULAE-20221031022). The rats were housed in a stable environment of 20–25 °C with 60 % humidity and had access to ample fresh water and food. A subcutaneous implant model was set up in 12 eight-week-old female SD rats. All scaffolds experienced ethylene oxide sterilization before being implanted into the rats. Surgeries for all animals were performed under a sterile condition. Rats were anesthetized with isoflurane, followed by shaving of their backs. In the middle of each rat's back, a cut about 2 cm in length was made longitudinally and connective tissues were bluntly dissected to create subcutaneous pouches on both sides of the vertebral column. Scaffolds were inserted into the subcutaneous pouches of the rats, after which incisions were closed using 4-0 sutures. The skin was cleaned post-operatively with a padded disinfectant. All the animals exhibited good post-operative health, and their wounds showed good healing conditions. After 2 and 4 weeks post-implantation, six rats from each interval were euthanized to extract skin samples from the location where the scaffold was placed. These samples were then subjected to immunofluorescence tests.

2.6.2. Osteogenesis in vivo

In this research, the osteogenesis efficacy of scaffolds with varying pore sizes was assessed using a calvarial defect model in New Zealand white rabbits. The rabbits were injected with sodium pentobarbital (0.02 g/kg) through the marginal ear vein. The calvarial region was subsequently shaved, disinfected, and the skin was exposed and incised. With the help of a trephine drill, a circular bone gap measuring 6 mm in diameter was fashioned on the cranium. Then, scaffolds of three different pore sizes (400 μm, 600 μm, and 800 μm) were implanted randomly into the defects, followed by wound suturing. The control defect was left without any scaffold implantation. For three days after implantation, daily injections of 1.0×10^4U/kg penicillin were administered. The post-surgical recovery of the animals was subsequently monitored. At 4 and 8 weeks after implantation, the rabbits were sacrificed. The specimens were retrieved from the tissues, dehydrated using gradient ethanol, followed by Micro-CT scanning. These samples were also subjected to H&E, Masson's trichrome, and immunohistochemistry (IHC) staining.

2.6.3. Imaging analysis

To observe the progression of new bone development and the healing of bone defects post-surgery, three specimens from each set were chosen at random for radial CT scans and subsequently at 4 and 8 weeks to study the callus expansion in the affected bone region. Following scanning, three-dimensional CT data were reconstructed using SkyScan NRecon software. CTAn software (SkyScan, Bruker Micro CT, Germany) was employed for image processing of the newborn bone zone as well as its covering regions, and ImageJ was used to manage statistical evaluation.

2.6.4. Histological analysis

After the CT scan procedure, the cranial samples were subjected to a 45-day decalcification process using EDTA (Servicebio, China). Samples from the center of the defect were harvested, specimens were extracted, encased in paraffin, and then cut into segments measuring 5 μm in thickness. Additionally, slices were exposed to IHC staining by incubating with anti-BMP-2 (Servicebio, China) and anti-RUNX2

Table 1
The primer sequence of all genes used in the Real-time PCR.

Gene	Forward	Reverse
Bmp-2	GTCTTCTAGTGTTGCTGCTTCCC	TCTCTGCTTCAGGCCAAACAT
Runx2	CAGTATGAGAGTAGGTGTCCCGC	AAGAGGGGTAAGACTGGTCATAGG
eNOS	TGTCCAACATGCTGCTGGAAATTG	AGGAGGTCTTCTTCCTGGTGATGCC
VEGF	TATGCGGATCAAACCTCACCA	CACAGGGATTTTTCTTGTCTTGCT
CCR7	TGTACGAGTCGGTGTGCTTC	GGTAGGTATCCGTCATGGTCTTG
INOS	CACCAAGCTGAACTTGAGCG	CGTGGCTTTGGGCTCCTC
ARG1	CCAGAAGAATGGAAGAGTCAGTGT	GCAGATATGCAGGGAGTCACC
CD206	CTCTGTTCAGCTATTGGACGC	CGGAATTTCTGGGATTCAGCTTC
GAPDH (mouse)	TGACCACAGTCCATGCCATC	GACGGACACATTGGGGGTAG
GAPDH (human)	GATTTGGTCGTATTGGGCG	CTGGAAGATGGTGATGG

(Servicebio, China).

2.6.5. Immunofluorescence staining

In vitro, RAW264.7 cells were incubated with scaffolds over a span of three days. Following to this period, the culture medium was discarded. The cells were then rinsed thrice using PBS, fixed for an hour using 4 % paraformaldehyde, and then decalcified for 4 weeks using EDTA. The samples were subjected to a gradient ethanol dehydration process, then encased in paraffin, and 5 μm-thick sections of parallel to the skull were prepared. RAW264.7 cells were permeabilized with 0.2 % Triton X-100 for 10 min. The sections were sealed with a blocking solution at room temperature for 1 h, then transferred to a primary antibody of F4/80 (Servicebio, China) and incubated overnight at 4 °C. After being washed with PBS, the secondary antibody was applied for another incubation with cells at room temperature for 1 h and then DAPI was employed for counterstaining. Finally, an anti-fluorescence quenching agent was used to seal the slides.

Immunofluorescence staining was performed on the subcutaneously implanted sample sections to analyze macrophage polarization and endothelial cell phenotype. After routine deparaffinization, sections were treated with in an antigen retrieval kit and then boiled in a microwave for 30 min. Sections, when cooled to room temperature, were washed with PBS on a shaker for destaining purposes. To prevent non-specific primary antibody binding, sections were placed in 20 % goat serum and 0.1 % Triton X-100 in PBS for 1 h. The sections were incubated with the primary antibody overnight. Then specimens were stained with two sets of typical markers, which are anti-iNOS antibody (Servicebio, China), and anti-ARG-1 antibody (Servicebio, China), anti-VEGF antibody (Servicebio, China), and anti-eNOS antibody (Servicebio, China) antibodies respectively. The sections were then washed with PBS and exposed to secondary antibodies that were labeled with fluorescence.

2.7. Statistical analysis

Data were evaluated using the GraphPad Prism 8. The values are quantitatively presented as means ± SD. After confirming that the data conformed to a normal distribution, we employed one-way ANOVA to determine statistical differences. Additionally, Tukey's method was used to compare different groups. All data are expressed as the means ± SD. *$p < 0.05$, **$p < 0.01$, ***$p < 0.001$ and ****$p < 0.0001$; ns indicates no significant difference.

3. Results and discussion

3.1. Material characteristics

The pore sizes for each scaffold group matched the predetermined values of 404.8 ± 44.68 μm, 625.5 ± 38.58 μm, and 782.0 ± 40.87 μm. The scaffolds surfaces had a medium roughness, which is favorable for cell attachment and proliferation (404.8 ± 44.68 μm, 625.5 ± 38.58 μm, 782.0 ± 40.87 μm) (Fig. 1A).

In vitro, we cultured RAW264.7 cells using scaffolds of varying pore sizes. Using the SEM, we examined the cells on the scaffolds and found that the scaffold surface, rather than the inner pores, displayed a consistent roughness, which is beneficial for enhancing cell adhesion to the scaffold and promoting cell proliferation. SEM results showed that 3 days after cultivation, the cells could uniformly adhere to the surfaces of all scaffold types, displaying elongated and stretched morphologies. As shown in the figure, macrophages on the surfaces of the three scaffold types exhibited no significant morphological differences (Fig. 1B). This suggests that the precision and controllability of the manufacturing process would contribute to consistent roughness of the scaffolds, which enhances cell attachment and promotes cell proliferation [43].

Besides, it was demonstrated that the scaffold pore size influenced various mechanical and biological behaviors (Fig. 1C). The stress-strain curves indicate a reduction of compressive strength following increasing pore size. Notably, the 400 μm group scaffolds, characterized by smaller pore sizes, withstood the highest compressive strength levels. In contrast, the 800 μm group, featuring larger pores, exhibited the lowest rigidity. The smaller pores of the 400 μm scaffold might restrict cell growth and vascular formation within the pores, while the larger pores in the 800 μm scaffold might weaken its mechanical properties and stability. However, the rigidity of the scaffold has minimal impact on the polarization of macrophages. Our experimental objective aimed to ensure the scaffold maintained adequate rigidity, while maximizing the recruitment and adhesion of macrophages, and promoting vascularization. Regarding the composition, the primary presence of HA in crystalline form was confirmed by X-ray powder diffraction (XRD) results (Fig. 1D). In comparison to the typical JCPDS 09–0432 card, as shown in Fig. 1D, seven distinct HA peaks can be clearly identified (25.9, 31.8, 32.5, 32.9, 34.1, 46.6, and 49.6°). This indicates that scaffolds made of the same material did not have significant differences in their surface structures. Additionally, hydrophilicity is not affected by pore size (Fig. 1E). The scaffold exhibits good biocompatibility and thermal stability. Specific pore sizes display favorable mechanical properties. As a scaffold material already utilized clinically, studying the optimal pore size of this material aids in the customization of individualized scaffolds.

3.2. Inflammatory response of macrophages to the scaffold and its osteogenesis and angiogenesis effects

To study the impact of scaffolds with different pore sizes (400 μm, 600 μm, and 800 μm) on macrophage polarization, the gene expression of RAW 264.7 cells cultured on these scaffolds was measured by RT-qPCR. CCR7 and iNOS were designated as marker genes for M1 macrophages, while ARG-1 and CD206 were designated as marker genes for M2 macrophages (Fig. 2A). The research results indicated that, compared to the 400 μm and 800 μm scaffolds, macrophages on the 600 μm scaffold showed a significantly reduced expression of M1 marker genes, suggesting the 600 μm scaffold's capability to suppress macrophage pro-inflammatory responses. In terms of M2 marker gene expression, as the scaffold pore size increased, macrophages exhibited significant anti-inflammatory characteristics, most notably observed on the 600 μm scaffold. The physical limitations within smaller pore-sized scaffolds restricted the elongation of macrophages and the regulation of particular genetic signaling pathways [3,44].

Macrophages, as classic immune cells, play a significant role in promoting osteogenesis and angiogenesis locally after being induced to polarize on the scaffold, acting in conjunction with other osteoblasts and fibroblasts. To assess the impact of macrophage polarization on osteogenesis and vascular differentiation, we analyzed the levels of gene expression in BMSC and HUVEC that were cultured in conditioned medium. The specialized medium was derived from the culture fluid collected after co-culturing RAW 264.7 cells with scaffolds of different pore sizes for three days. As a result, we observed a significant upregulation of angiogenesis-related gene RNA expression (VEGF, eNOS) in HUVEC (Fig. 2C). VEGF participates in angiogenesis, the promotion of endothelial progenitor cells recruitment and homing , and endothelial cell proliferation and sprouting [45–47]. Endothelial nitric oxide synthase (eNOS) contributes to production of nitric oxide (NO) to be involved in VEGF-induced vascularization in coronary vessels, in blood coagulation triggered by the activated platelets, and in the relaxation of vascular smooth muscle through a signal transduction pathway modulated by cGMP [48,49]. This implies that scaffold architectures at the micro and nano scale have the potential to improve vascular differentiation by modulating the macrophage immune microenvironment [50,51].

In addition, it can be observed that the conditioned medium has a notable impact on increasing the RNA expression of osteogenic genes (BMP-2, COL1) in BMSCs (Fig. 2D). BMP-2 promoted osteoblastic differentiation, and alkaline phosphatase activity. COL1, being a fibrous

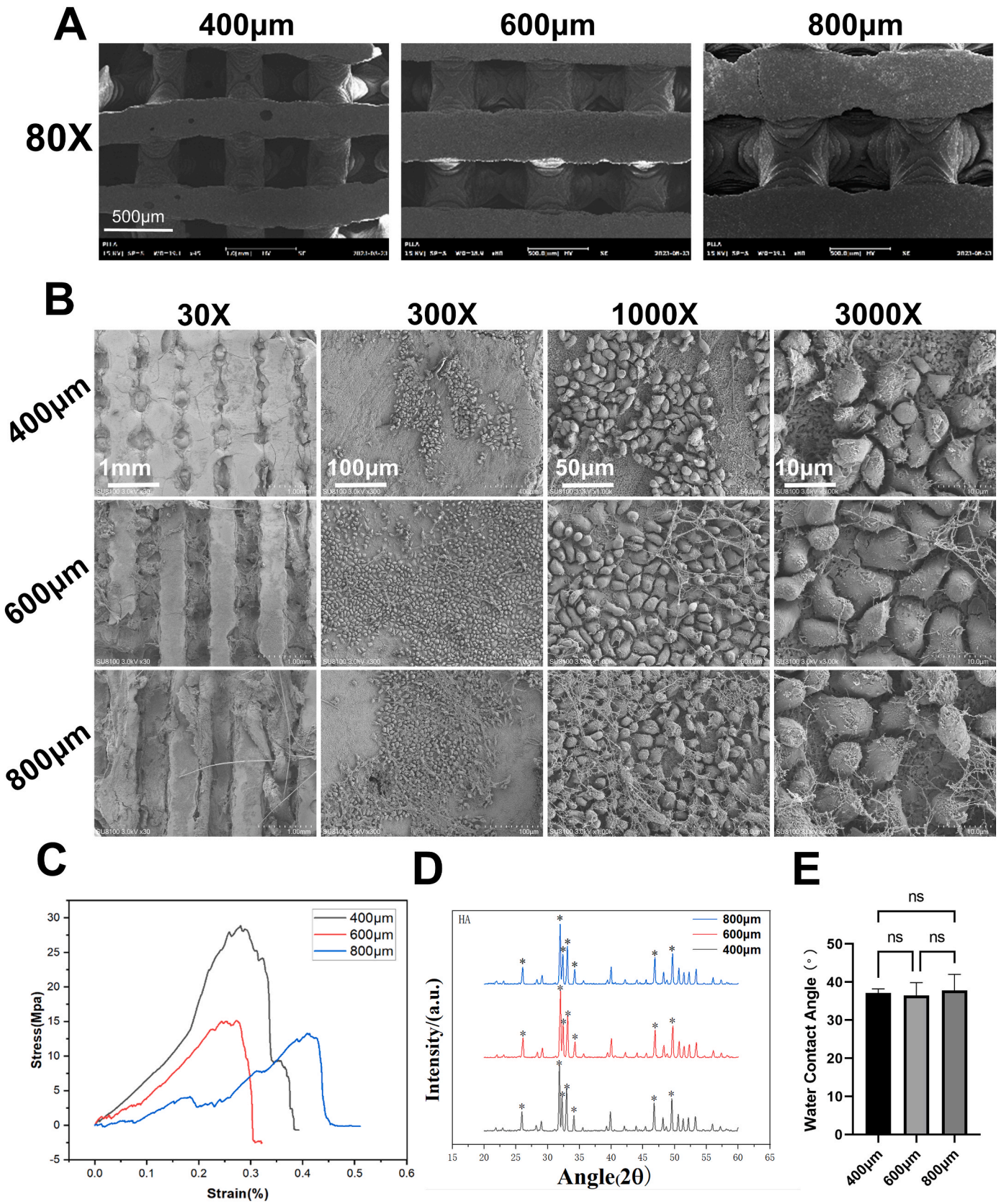

Fig. 1. Characterization of scaffolds. (A) SEM images of the 400 μm, 600 μm and 800 μm scaffolds. (B) Under gold-sputtered microscopy, adhesion of macrophages on the surface of the 400 μm, 600 μm, and 800 μm scaffolds. Characterization of 3D printed DLP scaffolds with distinct pore sizes (3 days). (C) Compressive modulus. (D) XRD patterns of the 3D printed DLP scaffold. (E) Hydrophilicity of the scaffold. n = 3 for biological replicates. SEM: scanning electron microscopy, DLP：digital light projection, XRD: X-ray powder diffraction.

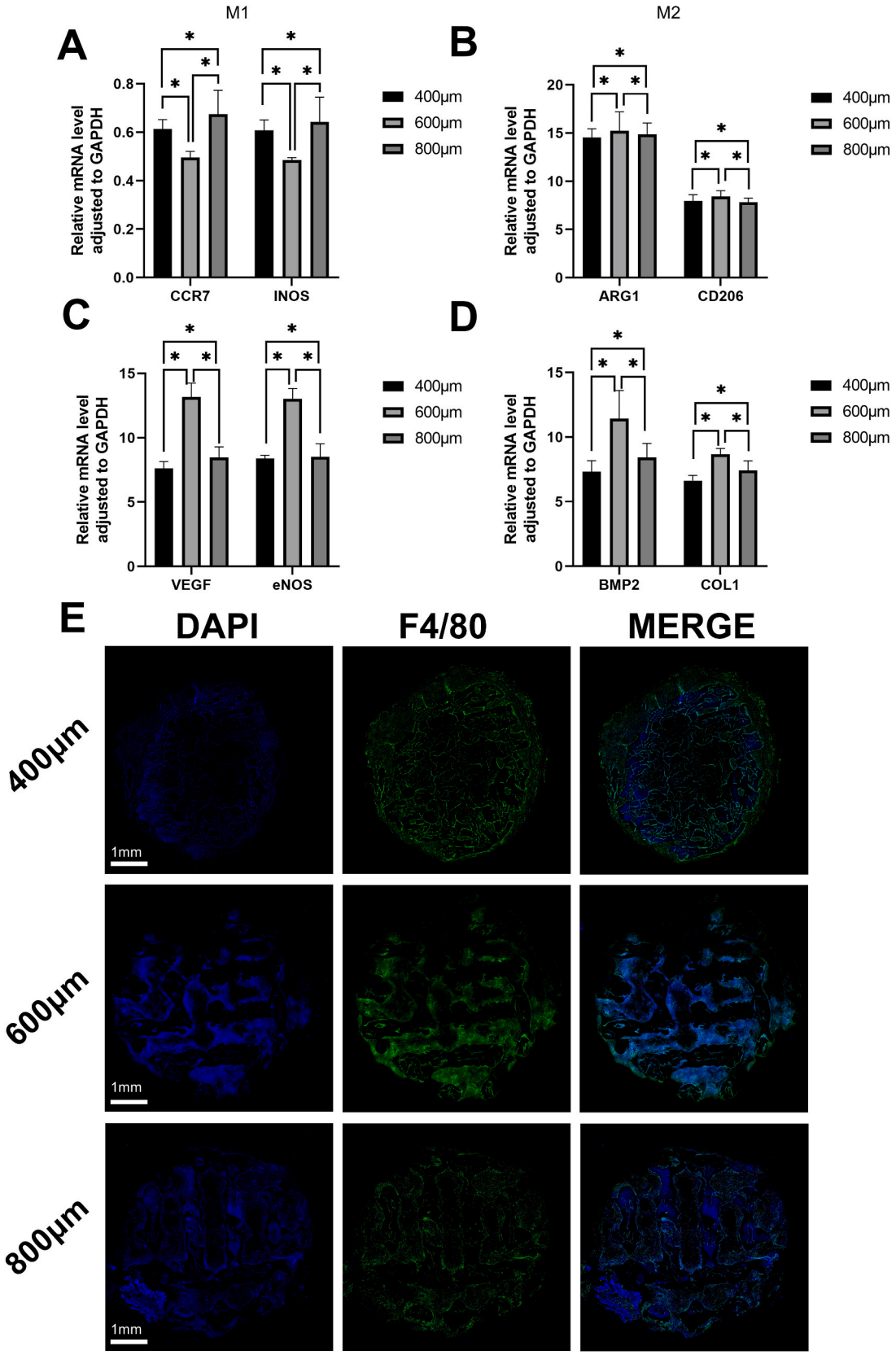

Fig. 2. Inflammatory response of macrophages to the scaffold and its osteogenesis and angiogenesis effects. (A–B) RT-qPCR analysis showed gene expression of polarized RAW 264.7 cells. CCR7 and iNOS were used as markers for M1 polarization; ARG-1 and CD206 were used as markers for M2 polarization (C–D) Expression of angiogenic genes (VEGF and eNOS) of HUVECs and osteogenic genes (BMP-2 and COL1) of BMSCs cultured in RAW 264.7 cells conditioned medium was analyzed by RT-qPCR. ns indicates no significant difference. (E–F) In vitro evaluation of scaffold cell compatibility and cell distribution using DAPI (nuclear staining) and F4/80 (macrophage marker). n = 3 for biological replicate.

collagen protein, is among the most abundant and crucial protein in the human body, which are particularly important for skin, bones, and connective tissue. The 600 μm group demonstrated higher osteogenic capabilities compared to the 400 μm and 800 μm groups. This indicates that specific micrometer-sized pore structures can enhance bone formation by modulating the immune microenvironment [52].

By employing immunofluorescence, we utilized F4/80 as a marker for macrophages to identify the attachment of macrophages on scaffolds of varying pore sizes (Fig. 2E). Immunofluorescent images revealed that regardless of pore size, macrophages uniformly covered the scaffold surface and occupied all areas, indicating good bioactivity and biocompatibility of the scaffold.

3.3. DEGs comparison revealed a scaffold characteristic

To well know the role of pore size in macrophage polarization, expressed genes were obtained by RNA-Seq in the control group, 400 μm, 600 μm, and 800 μm groups at 1 week after co-culture. After the DEGs were evaluated, it was discovered that in the 400 μm group compared to the control group, 708 DEGs were up-regulated and 668 DEGs were down-regulated. (Fig. 3A). Besides, 482 up-regulated DEGs and 437 down-regulated DEGs were observed in 600 μm group in comparison to the control group (Figs. 3B), and 258 up-regulated DEGs and 366 down-regulated DEGs were found in 800 μm group in comparison to the control group (Fig. 3C).

A heatmap is used to display the distribution of all DEGs in each group. Although various pore sizes can promote macrophage polarization, their underlying mechanisms may not be the same (Fig. 3D). According to the Venn diagram, the three groups shared 216 genes, while there was a significant difference in gene expression among these groups. There were 100 genes expressed differentially between the 600 μm and 800 μm group, 65 genes expressed differentially between 800 μm and 400 μm group, and 338 different genes between 400 μm and 600 μm group (Fig. 3E). The verification of the macrophage polarization mechanism is based on gene sequencing, and both hypoxia-inducible factor-1α (HIF-1α) and interferon−beta (IFN-β) have the highest expression in the 600 μm groups (Fig. 3F–G). HIF-1α and IFN-β were found to be important in M2 polarization [53,54].

Despite the histological evidence of macrophage polarization following scaffold implantation (Fig. 4), the precise functions of DEGs and their association with macrophage polarization remained uncertain. This study utilized GO enrichment to examine the role of DEGs in biological processes, cellular components, and molecular functions. Comparing 600 μm to the 400 μm group, chromosome segregation, nuclear chromosome segregation and interferon−beta production were up-regulated in 600 μm group. Defense response to bacterium, T cell activation involved in immune response, transition metal ion transport, defense response to gram−positive bacterium were down-regulated in 600 μm group (Fig. 4A–B). Comparing 800 μm to the 600 μm group, axonogenesis, myeloid cell differentiation and osteoclast differentiation were up-regulated, and ribonucleoprotein complex biogenesis, response to fluid shear stress and response to hyperoxia were down-regulated in the 800 μm group (Fig. 4C–D). The KEGG database was used for pathway analysis of DEGs. Comparing 600 μm to the 400 μm group, base excision repair, mismatch repair, and DNA replication were up-regulated and ferroptosis, carbon metabolism and lysosome were down-regulated in the 600 μm group (Fig. 4E–F). Cocaine addiction and spinocerebellar ataxia were upregulated, and Ribosome, diabetic cardiomyopathy and oxidative phosphorylation were down-regulated in the 800 μm group in comparison to 600 μm group (Fig. 4G–H).

Data gathered from 400 μm, 600 μm, 800 μm and control group were analyzed in the Gene Ontology (GO) database (Fig. 5A–F). Comparing 400 μm, 600 μm and 800 μm to the control group, ribonucleoprotein complex biogenesis was up-regulated and peptidyllysine modification were down-regulated. In addition, the pathway enrichment of differentially expressed genes were determined by KEGG up and down pathway enrichment analysis (Fig. 5G-L). The comparison of the 400 μm, 600 μm, and 800 μm groups revealed that the main pathways of DEGs were associated with amino acid biosynthesis and the HIF-1 signaling pathway.

The aforementioned results from GO and KEGG results align with the vitro experiments. In the 600 μm group, macrophage polarization to M2 was observed starting from day 3. In the 600 μm group, macrophages exhibit a pronounced M2 polarization, which could result from the up-regulated production of IFN-β, increase of HIF-1α level, and decrease of defense response to microorganisms [53–55]. IFN-β participates in JAK1-STAT6 pathway and induces IL-10 production, which promote M2 polarization and drive a transition from an M1 to an M2 phenotype [3,56]. This activation diminishes tissue damage stemming from immune responses. Conversely, in the 800 μm group, macrophages display reduced levels of oxidative phosphorylation, a key determinant in limiting their shift towards M2 polarization [57,58]. During the proliferation and polarization process of macrophages, the enrichment of GO terms and KEGG pathways related to glycolysis, cell proliferation, and amino acid metabolism was observed. In summary, the primary functions of scaffolds in promoting macrophage polarization are reflected in macrophage replication and amino acid metabolism. (Fig. 5A–C).

3.4. Evaluation of macrophage polarization and its angiogenesis effects in the rat subcutaneous implantation model

In order to assess the effect of scaffolds featuring varying pore dimensions on the immune response and vascular formation in vivo, we subcutaneously implanted scaffolds of three pore sizes (400 μm, 600 μm, and 800 μm) into the backs of rats. Scaffolds were removed at the 2nd and 4th weeks, and immunofluorescence analysis showed that, at 2 weeks post-implantation, the number of M1 polarized macrophages in the 600 μm scaffold was significantly lower than in the other two scaffolds, while the count of M2 polarized macrophages was significantly higher. This indicates that, even under complex in vivo conditions, the scaffold can effectively recruit and induce macrophage differentiation and influence the immune microenvironment (Fig. 6A–B). According to enrichment analysis, we assumed that the 600 μm scaffold modulates macrophage polarization through upregulation of IFN-β production, HIF-1α level and oxidative phosphorylation [53,54,59].

After two weeks of implantation, we analyzed the indicators of vasculogenesis, specifically VEGF and eNOS, within the specimens (Fig. 6C–F). The results demonstrated that endothelial cells assembled on the surfaces of all three types of scaffolds and were evenly distributed around the pore structures and the periphery of the materials. The 600 μm scaffold exhibited the most optimal endothelial cells recruitment, assembly and sprouting. This indicates that the early angiogenesis on the material surface is closely related to macrophage polarization. In the process of tissue regeneration, the biological scaffold stimulates angiogenesis indirectly by regulating the polarization of macrophages towards M2 [47,60]. Four weeks after implantation, the trend of endothelial cells assembly in the three scaffolds showed no significant changes compared to the 2-week post-implantation (Fig. 6G–J). The 600 μm scaffold continued to demonstrate the most optimal angiogenesis effect, providing optimal conditions for the later bone generation, while there was no notable distinction between the 400 μm and 800 μm scaffolds [61].

3.5. Evaluation of bone regeneration in the rabbit skull defect mode

Four and eight weeks after implantation, we performed immunofluorescence and immunohistochemistry analyses on the cranial specimens to assess the impact of different sizes of scaffold pores on vascular formation and new bone generation (Fig. 7). We detected the same angiogenesis markers, VEGF and eNOS, and new bone formation markers, BMP-2 and runt-related transcription factor 2 (RUNX2) (Fig. 8). RUNX2 is one of the key transcription factors in the process of

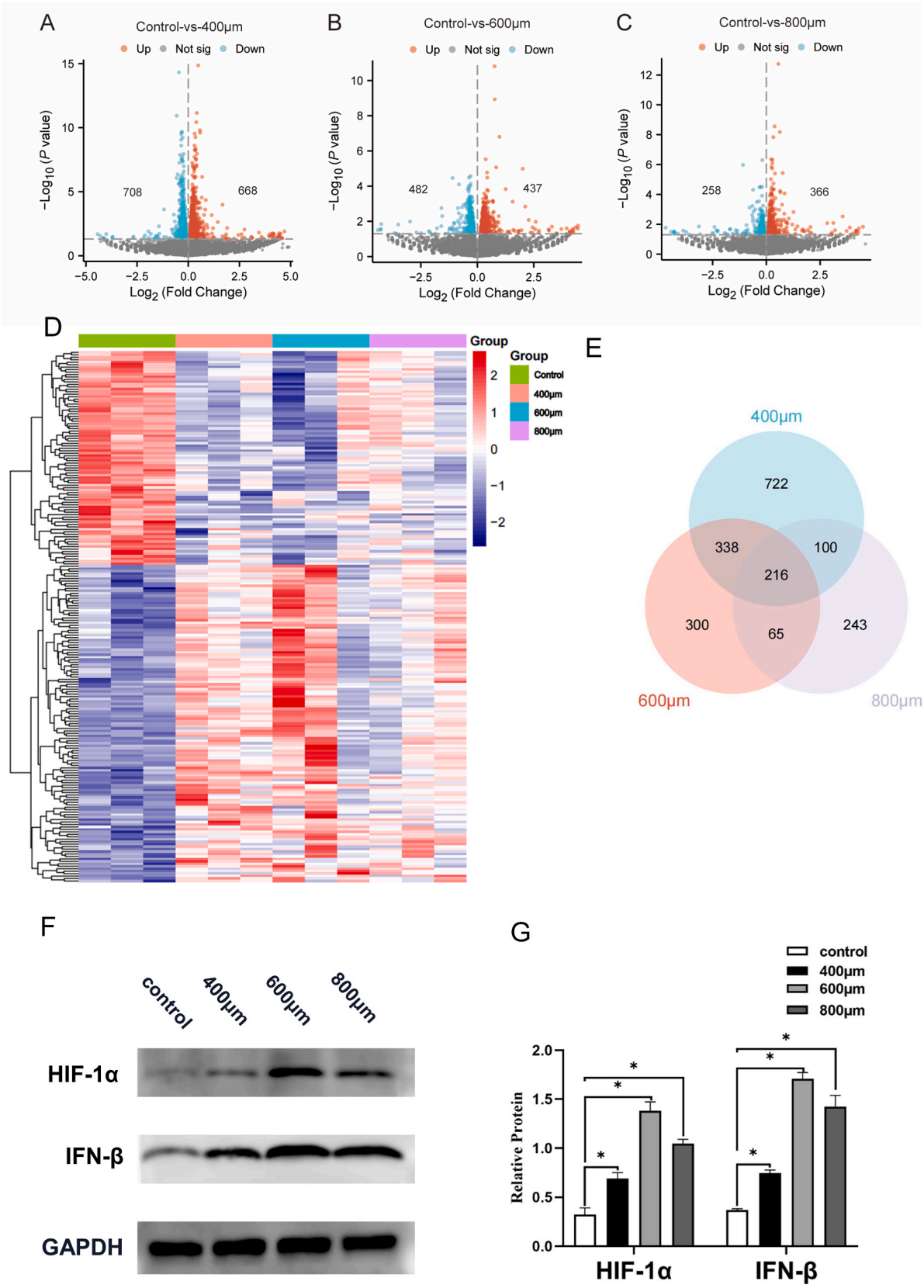

Fig. 3. DEGs Comparison Revealed a Scaffold Characteristic (A-C) Volcano plots displaying the expression levels of diverse genes across distinct samples (n = 3). (D) Heat Map displaying the differentially expressed genes associated with macrophage polarization in comparison of different groups. (E) A Venn diagram illustrating the variation in gene expression among various samples. (F–G) Three scaffolds were cultured with macrophages for three days, and changes in the expression levels in relative genes of IFN-β and HIF-1 α. IFN-β: Interferon-β, HIF-1α: hypoxia-inducible factor-1α, DEGs: differentially expressed genes.

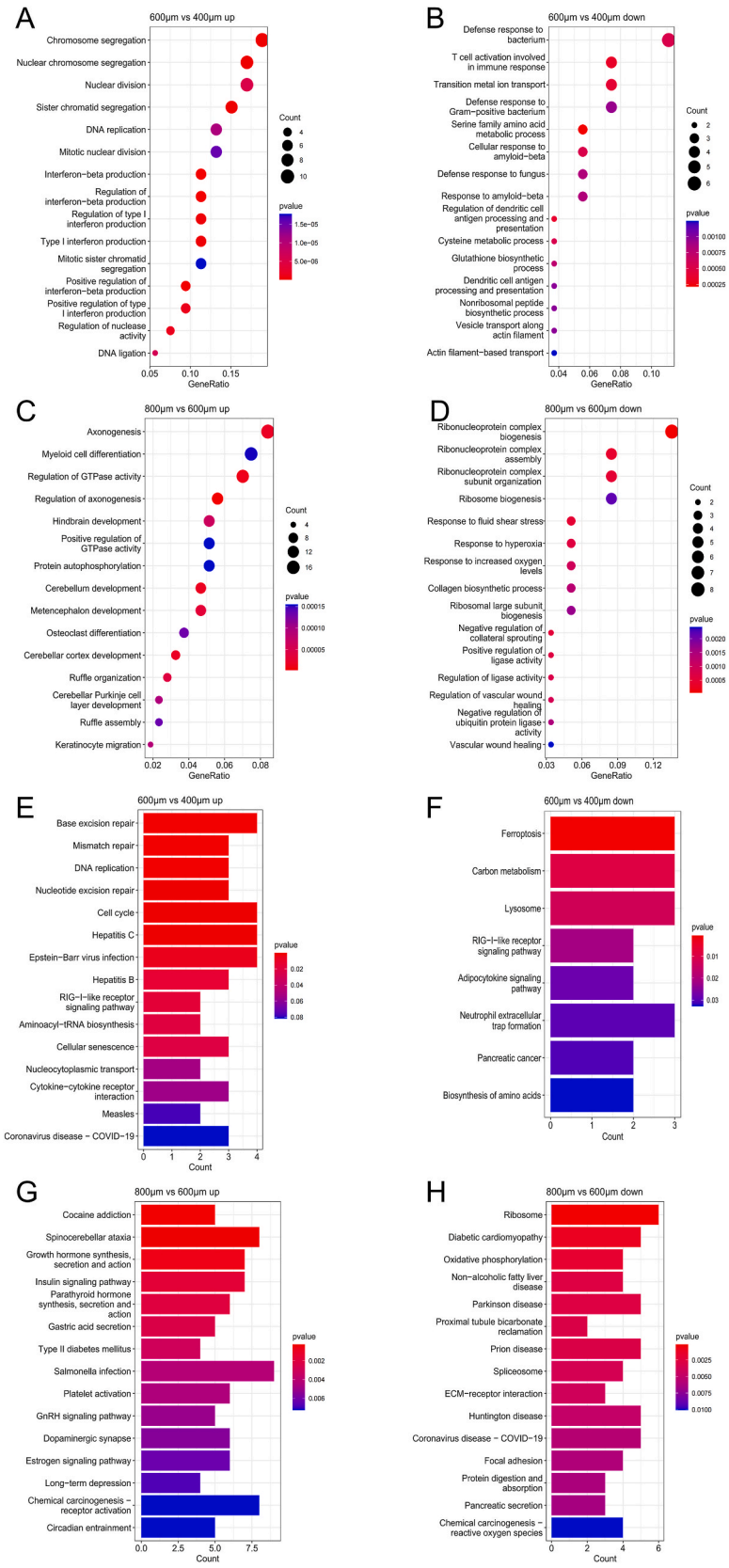

Fig. 4. GO enrichment analysis and KEGG enrichment analysis of DEGs in scaffold groups. (A–D) GO enrichment showed up-regulated and down-regulated expression in different groups compared with 600 μm group. (E–H) KEGG up-pathway and down-pathway enrichment analysis in different groups compared with 600 μm group. DEGs: differentially expressed genes.

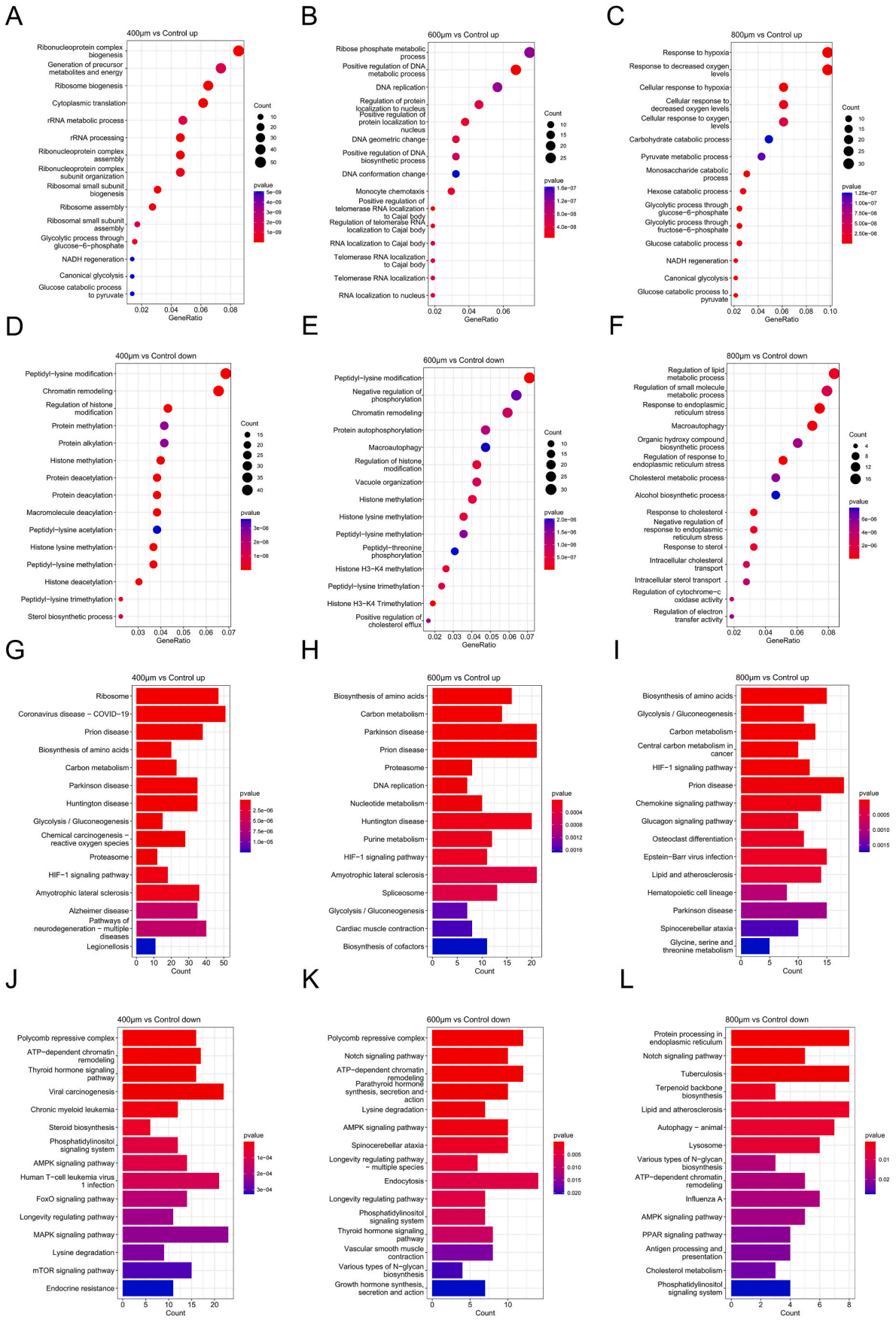

Fig. 5. DEGs Comparison and KEGG up and down pathway comparison in HA scaffold. (A–F) GO enrichment of the up-regulated and down-regulated expressions in different groups compared with control group. (G–L) KEGG up-pathway and down-pathway analysis compared with control group. HA: hydroxyapatite.

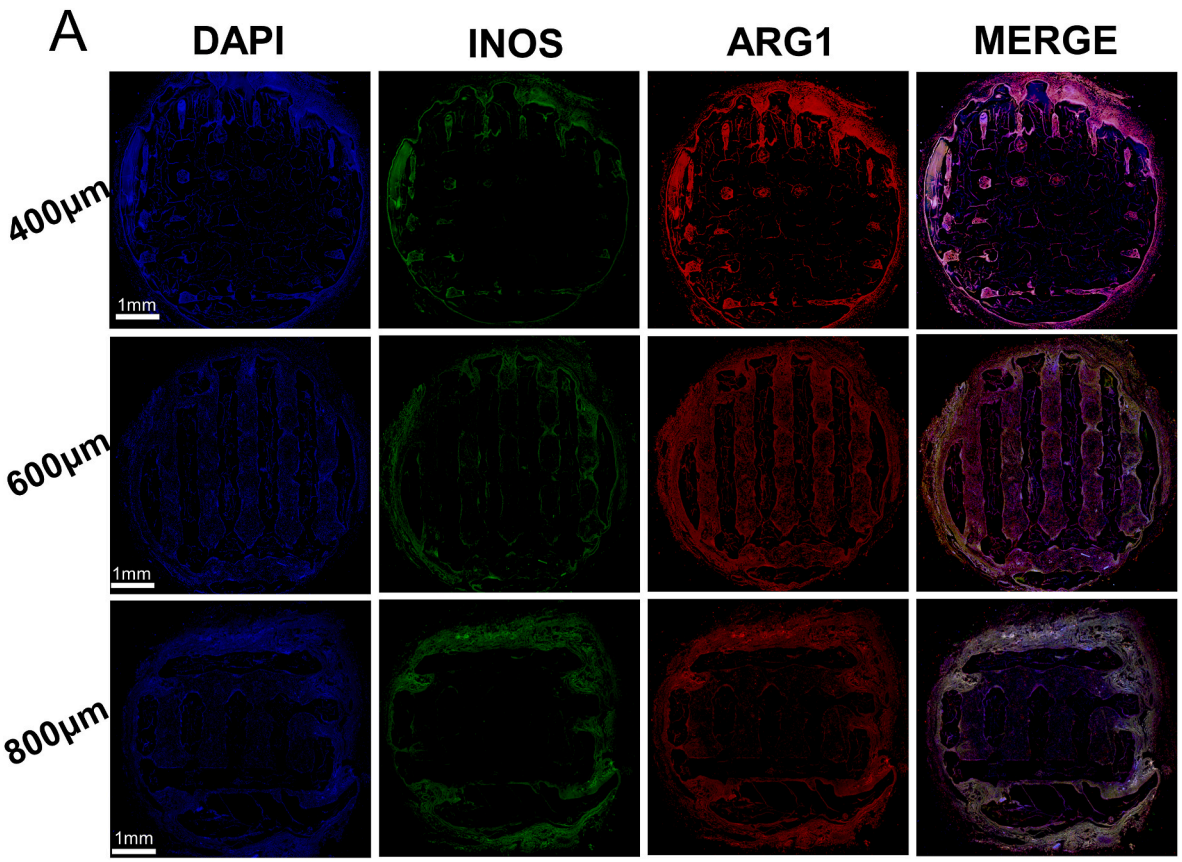

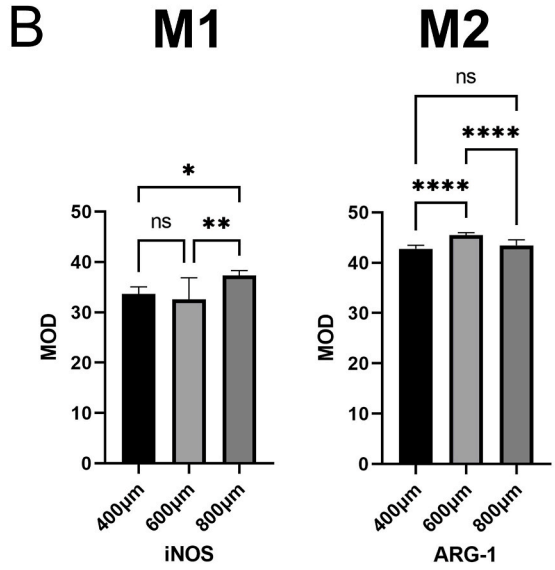

Fig. 6. Evaluation of macrophage polarization and its angiogenesis effects in the rat subcutaneous implantation model. (A–B) Immunofluorescence staining images show the response of host macrophages to the 400 μm, 600 μm, and 800 μm scaffolds 2 weeks post-implantation, highlighted by DAPI (blue for cell nuclei), INOS (green for M1 polarized macrophages), and ARG1 (red for M2 polarized macrophages). Accompanied by statistical analysis. (C–F) Immunofluorescence staining images illustrate the angiogenic response to the 400 μm, 600 μm, and 800 μm scaffolds 2 weeks after implantation, emphasizing DAPI (blue for cell nuclei), eNOS (green marker for endothelial cells), and VEGF (red marker for angiogenesis). This is complemented by a statistical evaluation. (G–J) Immunofluorescence staining images showcase the angiogenic response to the 400 μm, 600 μm, and 800 μm scaffolds 4 weeks post-implantation, highlighting DAPI (blue for cell nuclei), eNOS (green marker for endothelial cells), and VEGF (red marker for angiogenesis). Accompanied by statistical analysis. n = 3 for biological replicates. DAPI: dihydrochloride.

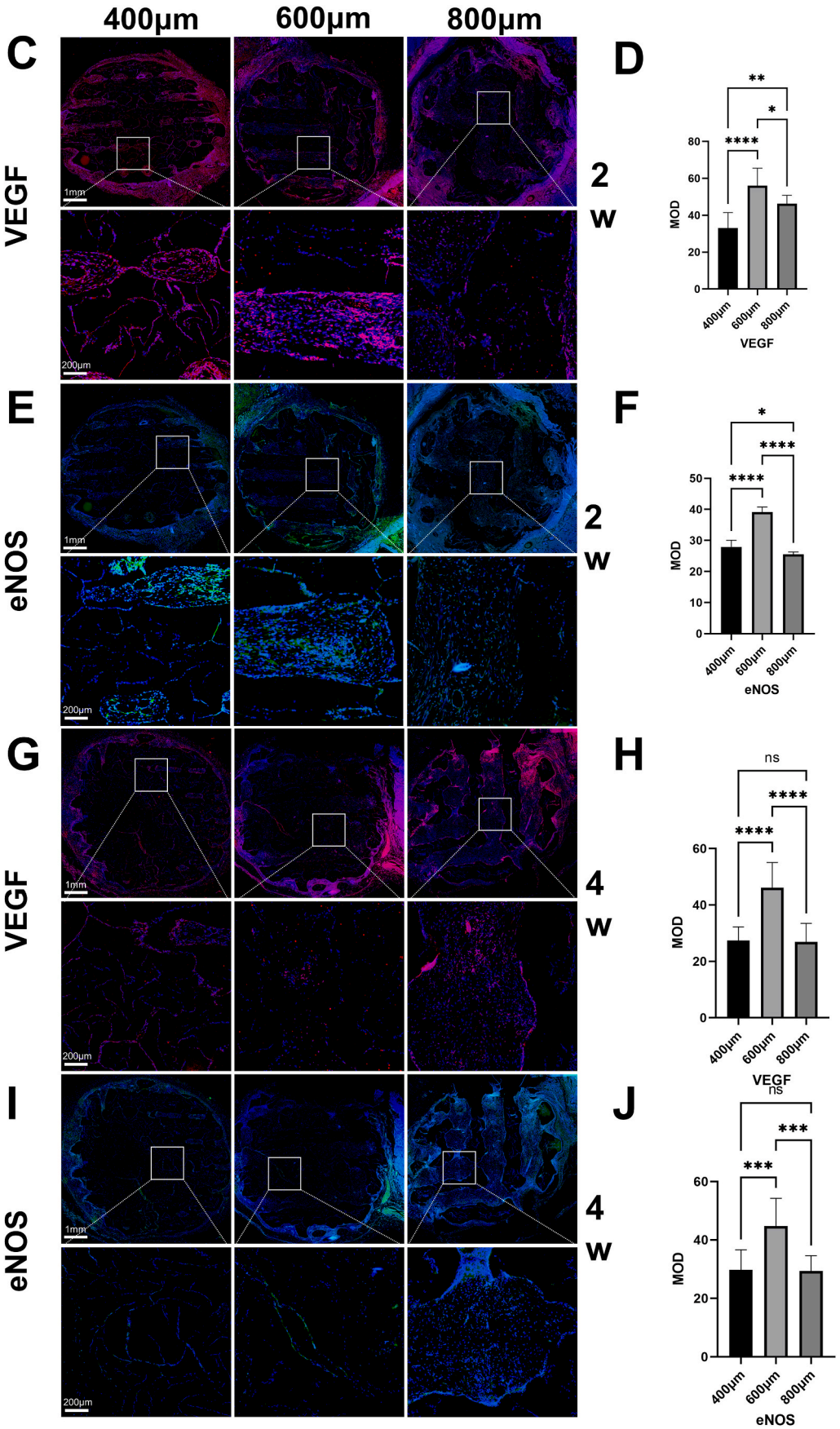

Fig. 6. (*continued*).

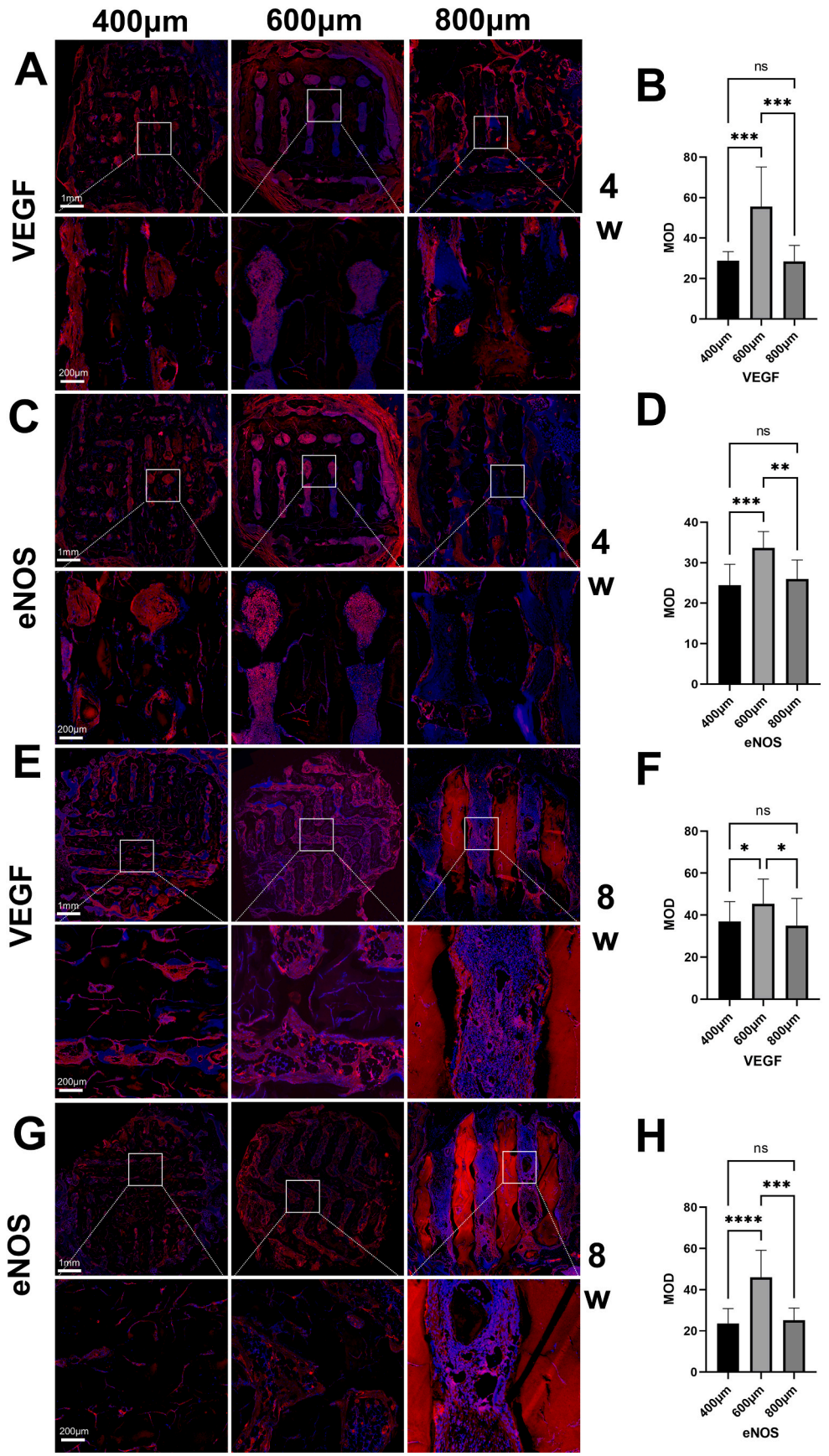

(caption on next page)

Fig. 7. Evaluation of vascularization in the rabbit skull defect mode. (A–D) Immunofluorescence staining images show the vascularization of the 400 μm, 600 μm, and 800 μm scaffolds 4 weeks post-implantation, highlighting DAPI (blue for cell nuclei), eNOS (green marker for endothelial cells), and VEGF (red marker for angiogenesis). Accompanied by statistical analysis. (E–H) Immunofluorescence staining images illustrate the vascularization of the 400 μm, 600 μm, and 800 μm scaffolds 8 weeks after implantation, emphasizing DAPI (blue for cell nuclei), eNOS (green marker for endothelial cells), and VEGF (red marker for angiogenesis). This is complemented by a statistical evaluation. n = 3 for biological replicates.

osteoblast differentiation and osteogenesis. Its primary function is to regulate cell division and to interact with other transcription factors during differentiation. Compared to the 4-week implantation, the 600 μm scaffold group continued to exhibit the highest number of newly formed vessels at week 8, with no notable distinction found between the scaffolds of 400 μm and 800 μm. Analyzing these observations, we considered the 600 μm scaffold group to have the highest level of M2 polarization in macrophages, which is beneficial for vascular formation; The 400 μm scaffold group's smaller pores hindered cell infiltration and distribution, and fewer vessels were generated, hindering oxygen and nutrient exchange; Besides promoting cell infiltration, the appropriate pore size structure is also conducive to the delivery of nutrients and oxygen, as well as the discharge of waste, thereby improving cell survival rates and tissue regeneration capabilities [62]. The 800 μm scaffold group has excessively large pores, resulting in more oxygen permeation and failing to establish a low-oxygen environment, The anaerobic glycolysis process is diminished, leading to reduced lactate levels, which in turn reduces the generation of blood vessels and fibers. Moreover, the 600 μm scaffold group also exhibited greater new bone formation than compared to the remaining two groups at week 8. This suggests that M2-polarized macrophages play a significant role in osteogenesis [63,64].

In prior studies, the facilitative role of M2 macrophage polarization in nerve repair has also been highlighted [65]. Biomaterials have been designed to facilitate macrophage recruitment and subsequent polarization toward a healing-oriented state, which would promote Schwann cell (SC) migration, myelinization and axonal extension, and play a significant role in regulating and modifying nerve regeneration [66]. Besides, the secretion of VEGF by macrophages facilitated the neovascularization, acting as pathways to guide the migration of SC across the wound [67,68].

3.6. Histological analysis in the rabbit skull defect mode

To investigate the influence of scaffold pore sizes on neo-bone generation, we inserted scaffolds with diameters of 400 μm, 600 μm, and 800 μm into rabbit skull defect models and conducted H&E staining on these materials 4 weeks later. The H&E-stained images depicted the distribution patterns of the newly developed bone and osteoblasts inside the scaffold (Fig. 9A–B). In the groups with 600 μm and 800 μm scaffolds, neo-bone primarily settled within the scaffold's voids. Additionally, following the H&E staining of the materials at 4 weeks, we noticed that the neo-bone area in the 600 μm scaffold group was evidently larger than in the other two groups. Four weeks after the operation, results from H&E staining indicated the proliferation of inflammatory cells and fibrous tissues across the three groups. In the defect area, fibrous tissues and inflammatory macrophages intermingled, accompanied by minor neo-angiogenesis. The research findings suggest that the 400 μm scaffold group exhibited the least amount of neo-bone formation, aligning with prior immunohistochemical results. This indicates that in the early stages, sufficient space is necessary for the growth of inflammatory cells and fibroblasts, which is essential for tissue repair and bone regeneration.

Four weeks post-implantation, Masson' trichrome staining was undertaken. Masson' trichrome staining is capable of revealing collagen accumulations during the process of neo-bone growth, offering an indicator assessment of bone formation (Fig. 9C–D). The study results indicated a noticeably higher collagen deposition in the 600 μm scaffold group in comparison to the other two groups, suggesting its superior bone regeneration potential. The 400 μm scaffold group displayed minimal collagen accumulations, likely due to its smaller pore diameter obstructing cell entry and distribution. The 800 μm scaffold group also had diminished collagen depositions, possibly due to its larger pores not fostering the growth of a continuous fibrous matrix, resulting in fibers predominantly growing surrounding the pores instead of expanding internally.

3.7. Bone Regeneration Evaluated Using Micro-CT

The micro-CT 3D reconstructions and sagittal images showed incomplete mineralization within the scaffold pores (Fig. 10A–B). Minimal new bone formation was evident on the scaffold surface, while the edges showed no signs of new bone. At the junction of the pores, new bone growth was observed, penetrating into the scaffold. In the 600 μm group, more prominent new bone formation was evident, extending into the scaffold's inner region, aligning with the scaffold's pore design. Results from animal tests showed marked new bone growth in the 600 μm scaffold, a finding validated by the 3D visuals in the ROI area. Using CTAn software, CT data from each set of three scaffolds were assessed. The findings demonstrated that the 600 μm group displayed the top volume/total volume ratio (BV/TV) and trabecular thickness (Tb. Th) values and the bottom trabecular separation (Tb. Sp) values. The statistical significance of these differences compared to other groups suggests enhanced new bone formation in the 600 μm group (Fig. 10C–H).

In this experiment, we utilized rabbit skull samples, where each sample comprises four groups, all derived from the same rabbit. When comparing to radius defects models or femur defect models from different rabbits in the same period, the influence of extraneous factors becomes minimal, such as factors including inconsistent surgery times and varied post-operative recovery durations. Another critical factor to be considered is the inconsistency in the frequency of use and load-bearing between the front and hind legs. Given these considerations, the rabbit skull model emerges as a more reliable tool, which allows us to better compare the osteogenic and angiogenic effects of the three materials with the control group.

4. Conclusions

In conclusion, we have elucidated the optimal pore size for HA scaffolds. Our in vitro results highlight the scaffold's capacity to induce macrophage polarization and modulate the immune microenvironment. Similarly, in vivo findings underscore the distinctive roles of HA scaffolds with different pore sizes in promoting osteogenesis and angiogenesis. Specifically, scaffolds with smaller pore sizes impede local cell and blood vessel growth, decrease IFN-β production, and compromise M2 polarization. Conversely, larger pore sizes facilitate oxygen diffusion, suppressing the hypoxic HIF-1 pathway, which obstructs the shift toward M2 phenotype. Notably, the 600 μm scaffold exhibits the most favorable conditions for M2 polarization, consistently demonstrating superior osteogenic and angiogenic abilities both in vitro and in vivo. This investigation not only offers insights into optimizing scaffold structures for extensive bone tissue applications but also sheds light on the influence of pore size on the macrophage immune microenvironment.

Funding sources

This research was supported by the National Natural Science

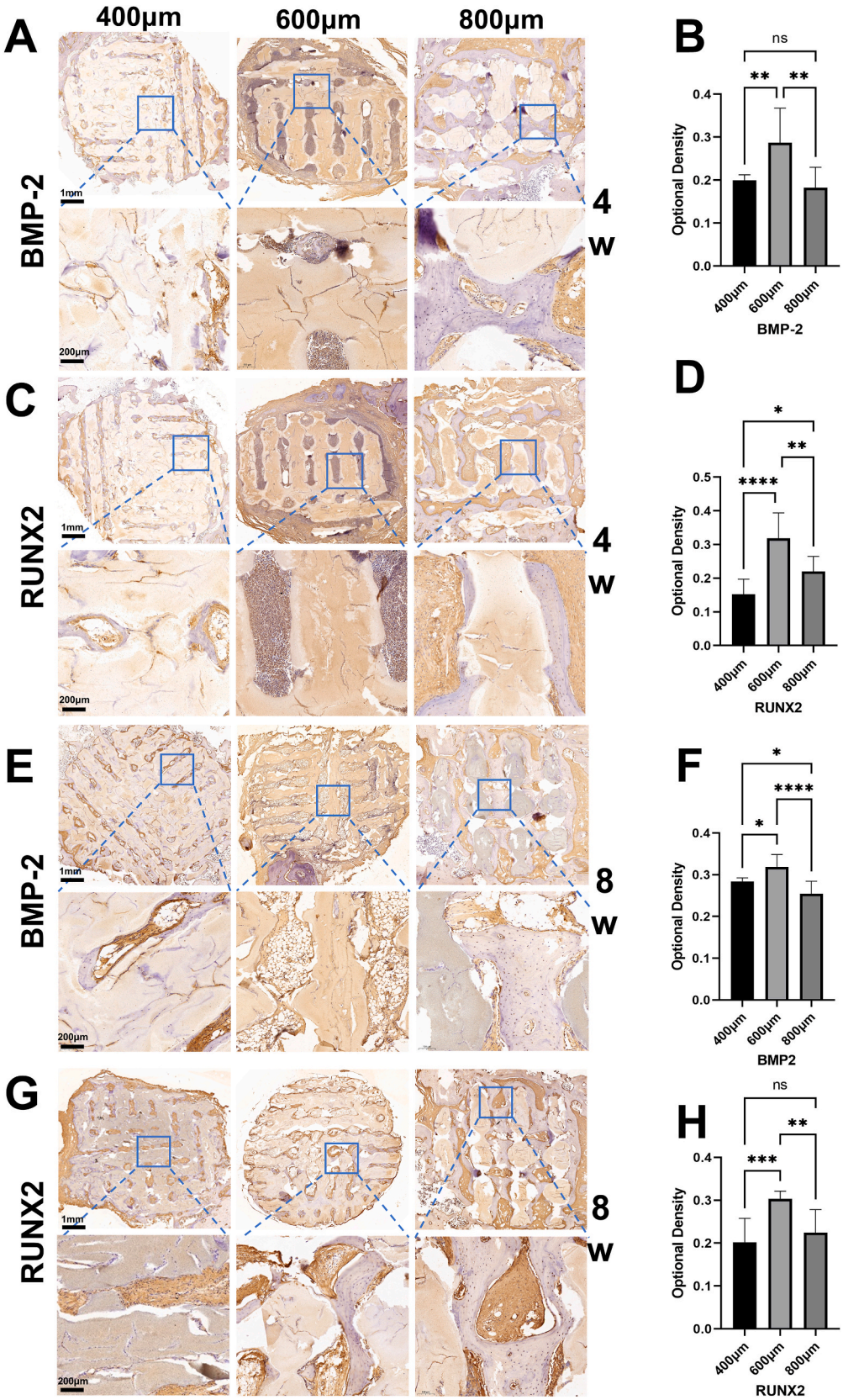

Fig. 8. Evaluation of osteogenesis in the rabbit skull defect mode. (A–D) Images from immunohistochemical staining depict the bone formation response of the 400 μm, 600 μm, and 800 μm scaffolds at 4 weeks after implantation, highlighting the BMP-2 and RUNX2 positive regions. (E–H) Images from immunohistochemical staining illustrate the bone formation response of the 400 μm, 600 μm, and 800 μm scaffolds at 8 weeks after implantation, emphasizing the BMP-2 and RUNX2 positive areas accompanied by a statistical evaluation. n = 3 for biological replicates.

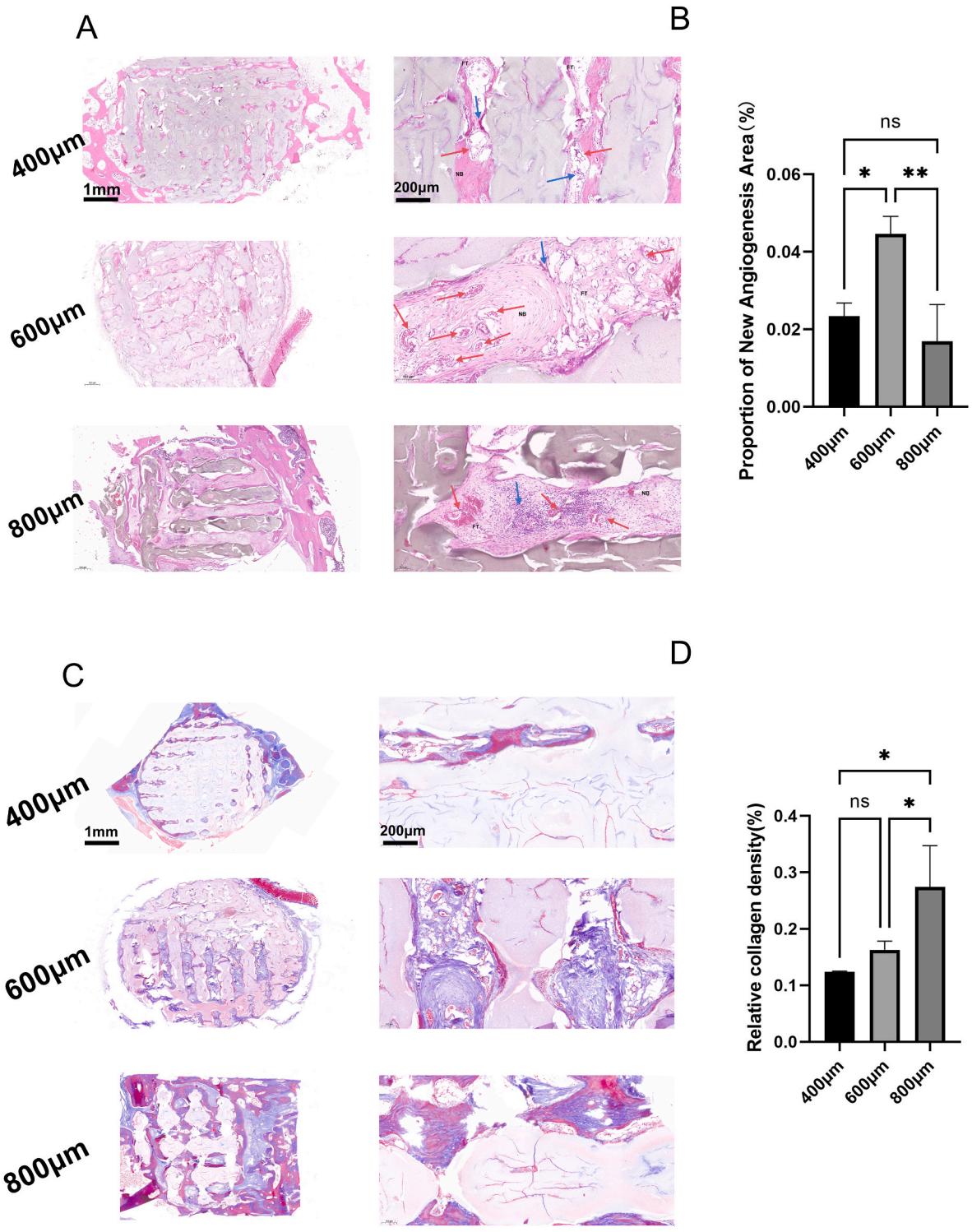

Fig. 9. Histological analysis in the rabbit skull defect mode. (A)Histological images from H&E staining depict the statistical evaluation of regenerated mineral tissue areas for 400 μm, 600 μm, and 800 μm scaffolds at 4 weeks after implantation. (B) Quantitative evaluation of the new angiogenesis area observed in H&E staining images. (C) Images of Masson's trichrome stain from scaffolds placed into rabbit skull defects at 4 weeks post-implantation. (D) Quantitative assessment of collagen regions within Masson's trichrome stained images from scaffolds, taken 4 weeks after implantation. Collagen density was represented as a percentage of the overall area. n = 3 for biological replicates. NB: new bones, FT: fibrous tissue; Red arrow: blood vessels; Blue arrow: inflammatory cells.

Foundation of China (82160354), the Jiangxi Provincial Department of Science and Technology (20224ACB206012, 20232BAB206036), the Health Commission of Jiangxi Province (202311845), and the Training plan for academic and technical leaders of major disciplines in Jiangxi Province (20204BCJL22047).

CRediT authorship contribution statement

Shilang Xiong: Investigation, Methodology, Writing - original draft. **Yinuo Zhang:** Investigation, Methodology, Writing - original draft. **Jianhua Zeng:** Methodology, Software. **Jingyu Zhou:** Validation, Software. **Shiwei Liu:** Project administration, Funding acquisition,

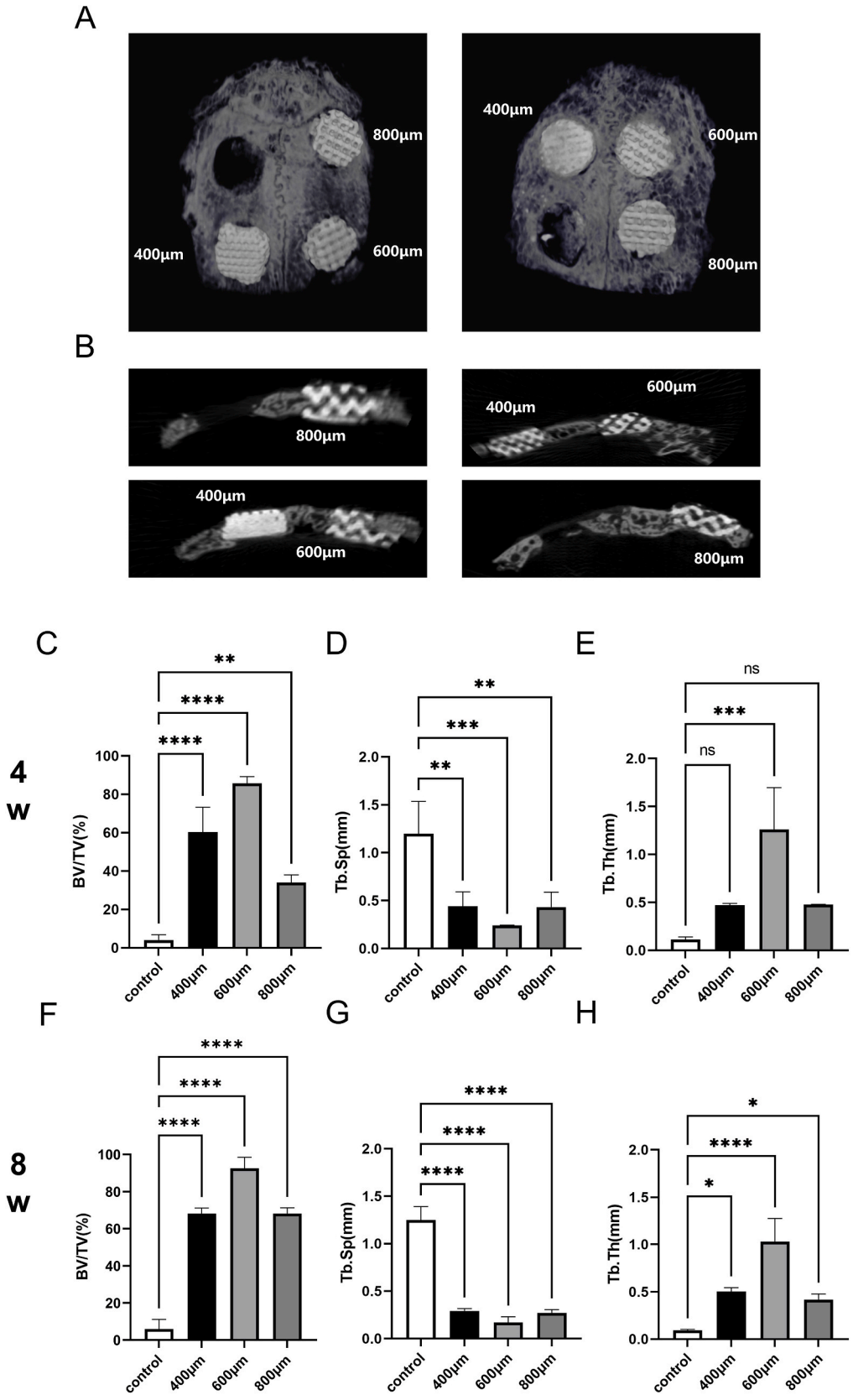

Fig. 10. Bone Regeneration Evaluated Using Micro-CT. (A)CT 3D macro-reconstructed images of 400 μm, 600 μm, and 800 μm scaffolds implanted in rabbit skull defect areas at 4 and 8 weeks. (B) Sagittal views of 400 μm, 600 μm, and 800 μm scaffolds in rabbit skull defect areas at 4 and 8 weeks. (C–D) Quantitative analysis of bone volume/total volume ratio (BV/TV), trabecular separation (Tb. Sp), and trabecular thickness (Tb. Th) from micro-CT data. n = 3 for biological replicates.

Resources, Data curation. **Peng Wei:** Validation, Visualization. **Hantian Liu:** Investigation, Methodology. **Feng Yi:** Investigation, Methodology. **Zongmiao Wan:** Funding acquisition, Resources. **Long Xiong:** Conceptualization, Funding acquisition, Supervision, Writing - review & editing. **Bin Zhang:** Conceptualization, Funding acquisition, Supervision. **Jingtang Li:** Conceptualization, Funding acquisition, Supervision.

Declaration of competing interest

The authors declare that they have no known competing financial interests or personal relationships that could have appeared to influence the work reported in this paper.

Data availability

No data was used for the research described in the article.

Acknowledgments

Scheme 1 was created with BioRender.com.

References

[1] S. Franz, et al., Immune responses to implants - a review of the implications for the design of immunomodulatory biomaterials, Biomaterials 32 (28) (2011) 6692–6709, https://doi.org/10.1016/j.biomaterials.2011.05.078.
[2] H. Takayanagi, Inflammatory bone destruction and osteoimmunology, J. Periodontal. Res. 40 (4) (2005) 287–293, https://doi.org/10.1111/j.1600-0765.2005.00814.x.
[3] B.N. Brown, et al., Macrophage polarization: an opportunity for improved outcomes in biomaterials and regenerative medicine, Biomaterials 33 (15) (2012) 3792–3802, https://doi.org/10.1016/j.biomaterials.2012.02.034.
[4] R. Langer, Perspectives and challenges in tissue engineering and regenerative medicine, Adv. Mater. 21 (32–33) (2009) 3235–3236, https://doi.org/10.1002/adma.200902589.
[5] G. Qian, et al., Enhancing bone scaffold interfacial reinforcement through in situ growth of metal-organic frameworks (MOFs) on strontium carbonate: achieving high strength and osteoimmunomodulation, J. Colloid Interface Sci. 655 (2023) 43–57, https://doi.org/10.1016/j.jcis.2023.10.133.
[6] C.Z.W. Lee, T. Kozaki, F. Ginhoux, Studying tissue macrophages in vitro: are iPSC-derived cells the answer? Nat. Rev. Immunol. 18 (11) (2018) 716–725, https://doi.org/10.1038/s41577-018-0054-y.
[7] A. Alaarg, et al., Applying nanomedicine in maladaptive inflammation and angiogenesis, Adv. Drug Deliv. Rev. 119 (2017) 143–158, https://doi.org/10.1016/j.addr.2017.05.009.
[8] T.J. Koh, L.A. DiPietro, Inflammation and wound healing: the role of the macrophage, Expet Rev. Mol. Med. 13 (2011) e23, https://doi.org/10.1017/S1462399411001943.
[9] J.M. Anderson, A. Rodriguez, D.T. Chang, Foreign body reaction to biomaterials, Semin. Immunol. 20 (2) (2008) 86–100, https://doi.org/10.1016/j.smim.2007.11.004.
[10] K.L. Spiller, T.J. Koh, Macrophage-based therapeutic strategies in regenerative medicine, Adv. Drug Deliv. Rev. 122 (2017) 74–83, https://doi.org/10.1016/j.addr.2017.05.010.
[11] Q. Zhang, et al., Effects of the fibrous topography-mediated macrophage phenotype transition on the recruitment of mesenchymal stem cells: an in vivo study, Biomaterials 149 (2017) 77–87, https://doi.org/10.1016/j.biomaterials.2017.10.007.
[12] S. Mukherjee, et al., Blended nanostructured degradable mesh with endometrial mesenchymal stem cells promotes tissue integration and anti-inflammatory response in vivo for pelvic floor application, Biomacromolecules 20 (1) (2019) 454–468, https://doi.org/10.1021/acs.biomac.8b01661.
[13] K. Li, et al., Sr-doped nanowire modification of Ca-Si-based coatings for improved osteogenic activities and reduced inflammatory reactions, Nanotechnology 29 (8) (2018) 084001, https://doi.org/10.1088/1361-6528/aaa2b4.
[14] R. Sridharan, et al., Biomaterial based modulation of macrophage polarization: a review and suggested design principles, Mater. Today 18 (6) (2015) 313–325, https://doi.org/10.1016/j.mattod.2015.01.019.
[15] D.M. Mosser, J.P. Edwards, Exploring the full spectrum of macrophage activation, Nat. Rev. Immunol. 8 (12) (2008) 958–969, https://doi.org/10.1038/nri2448.
[16] Z. Tang, et al., The material and biological characteristics of osteoinductive calcium phosphate ceramics, Regener Biomater 5 (1) (2018) 43–59, https://doi.org/10.1093/rb/rbx024.
[17] S. Feng, F. He, J. Ye, Hierarchically porous structure, mechanical strength and cell biological behaviors of calcium phosphate composite scaffolds prepared by combination of extrusion and porogen burnout technique and enhanced by gelatin, Mater. Sci. Eng., C 82 (2018) 217–224, https://doi.org/10.1016/j.msec.2017.08.039.
[18] M. Vallet-Regí, E. Ruiz-Hernández, Bioceramics: from bone regeneration to cancer nanomedicine, Adv. Mater. 23 (44) (2011) 5177–5218, https://doi.org/10.1002/adma.201101586.
[19] S.V. Dorozhkin, Bioceramics of calcium orthophosphates, Biomaterials 31 (7) (2010) 1465–1485, https://doi.org/10.1016/j.biomaterials.2009.11.050.
[20] B.H. Fellah, et al., Osteogenicity of biphasic calcium phosphate ceramics and bone autograft in a goat model, Biomaterials 29 (9) (2008) 1177–1188, https://doi.org/10.1016/j.biomaterials.2007.11.034.
[21] J. Li, et al., Tailoring materials for modulation of macrophage fate, Adv. Mater. 33 (12) (2021) e2004172, https://doi.org/10.1002/adma.202004172.
[22] J. Jiang, et al., Expanded 3D nanofiber scaffolds: cell penetration, neovascularization, and host response, Adv. Healthcare Mater. 5 (23) (2016) 2993–3003, https://doi.org/10.1002/adhm.201600808.
[23] K. Garg, et al., Macrophage functional polarization (M1/M2) in response to varying fiber and pore dimensions of electrospun scaffolds, Biomaterials 34 (18) (2013) 4439–4451, https://doi.org/10.1016/j.biomaterials.2013.02.065.
[24] J. Wang, et al., Nano-hydroxyapatite coating promotes porous calcium phosphate ceramic-induced osteogenesis via BMP/smad signaling pathway, Int. J. Nanomed. 14 (2019) 7987–8000, https://doi.org/10.2147/IJN.S216182.
[25] C.M. Niessen, D. Leckband, A.S. Yap, Tissue organization by cadherin adhesion molecules: dynamic molecular and cellular mechanisms of morphogenetic regulation, Physiol. Rev. 91 (2) (2011) 691–731, https://doi.org/10.1152/physrev.00004.2010.
[26] J.R. García, A.J. García, Biomaterial-mediated strategies targeting vascularization for bone repair, Drug Deliv. Transl. Research. 6 (2) (2016) 77–95, https://doi.org/10.1007/s13346-015-0236-0.
[27] J. Filipowska, et al., The role of vasculature in bone development, regeneration and proper systemic functioning, Angiogenesis 20 (3) (2017) 291–302, https://doi.org/10.1007/s10456-017-9541-1.
[28] X. Zheng, et al., Near-infrared-triggered dynamic surface topography for sequential modulation of macrophage phenotypes, ACS Appl. Mater. Interfaces 11 (46) (2019) 43689–43697, https://doi.org/10.1021/acsami.9b14808.
[29] M.M. Alvarez, et al., Delivery strategies to control inflammatory response: modulating M1-M2 polarization in tissue engineering applications, J. Contr. Release 240 (2016) 349–363, https://doi.org/10.1016/j.jconrel.2016.01.026.
[30] Y.Q. Goh, C.P. Ooi, Fabrication and characterization of porous poly(L-lactide) scaffolds using solid-liquid phase separation, J. Mater. Sci. Mater. Med. 19 (6) (2008) 2445–2452, https://doi.org/10.1007/s10856-008-3366-9.
[31] X. Wu, et al., Preparation of aligned porous gelatin scaffolds by unidirectional freeze-drying method, Acta Biomater. 6 (3) (2010) 1167–1177, https://doi.org/10.1016/j.actbio.2009.08.041.
[32] S.W. Suh, et al., Effect of different particles on cell proliferation in polymer scaffolds using a solvent-casting and particulate leaching technique, ASAIO J. (Am. Soc. Artif. Internal Org. 48 (5) (2002) 460–464, https://doi.org/10.1097/00002480-200209000-00003, 1992.
[33] C. Ji, et al., Fabrication of poly-DL-lactide/polyethylene glycol scaffolds using the gas foaming technique, Acta Biomater. 8 (2) (2012) 570–578, https://doi.org/10.1016/j.actbio.2011.09.028.
[34] A. Nandakumar, et al., Fabrication of bioactive composite scaffolds by electrospinning for bone regeneration, Macromol. Biosci. 10 (11) (2010) 1365–1373, https://doi.org/10.1002/mabi.201000145.
[35] B. Zhang, et al., Three-dimensional printing of large-scale, high-resolution bioceramics with micronano inner porosity and customized surface characterization design for bone regeneration, ACS Appl. Mater. Interfaces 14 (7) (2022) 8804–8815, https://doi.org/10.1021/acsami.1c22868.
[36] G. Qian, et al., 3D printed Zn-doped mesoporous silica-incorporated poly-L-lactic acid scaffolds for bone repair, Int. J. Bioprint 7 (2) (2021) 346, https://doi.org/10.18063/ijb.v7i2.346.
[37] H.D. Kim, et al., Biomimetic materials and fabrication approaches for bone tissue engineering, Adv. Healthcare Mater. 6 (23) (2017), https://doi.org/10.1002/adhm.201700612.
[38] B. Zhang, et al., 3D printing of customized key biomaterials genomics for bone regeneration, Appl. Mater. Today 26 (2022), https://doi.org/10.1016/j.apmt.2021.101346.
[39] A. Wubneh, et al., Current state of fabrication technologies and materials for bone tissue engineering, Acta Biomater. 80 (2018), https://doi.org/10.1016/j.actbio.2018.09.031.
[40] P. Bhattacharjee, et al., Silk scaffolds in bone tissue engineering: an overview, Acta Biomater. 63 (2017), https://doi.org/10.1016/j.actbio.2017.09.027.
[41] L. Zhang, et al., Three-dimensional (3D) printed scaffold and material selection for bone repair, Acta Biomater. 84 (2019) 16–33, https://doi.org/10.1016/j.actbio.2018.11.039.
[42] A. Shapouri-Moghaddam, et al., Macrophage plasticity, polarization, and function in health and disease, J. Cell. Physiol. 233 (9) (2018) 6425–6440, https://doi.org/10.1002/jcp.26429.
[43] S. Jiang, et al., Cryoprotectant enables structural control of porous scaffolds for exploration of cellular mechano-responsiveness in 3D, Nat. Commun. 10 (1) (2019) 3491, https://doi.org/10.1038/s41467-019-11397-1.
[44] N. Jain, V. Vogel, Spatial confinement downsizes the inflammatory response of macrophages, Nat. Mater. 17 (12) (2018) 1134–1144, https://doi.org/10.1038/s41563-018-0190-6.
[45] T. Liu, et al., Endothelialization of implanted cardiovascular biomaterial surfaces: the development from in vitro to in vivo, J. Biomed. Mater. Res. 102 (10) (2014) 3754–3772, https://doi.org/10.1002/jbm.a.35025.
[46] P. Carmeliet, Mechanisms of angiogenesis and arteriogenesis, Nat. Med. 6 (4) (2000) 389–395, https://doi.org/10.1038/74651.

[47] W. Risau, I. Flamme, Vasculogenesis, Annu. Rev. Cell Dev. Biol. 11 (1995) 73–91, https://doi.org/10.1146/annurev.cb.11.110195.000445.
[48] C. Urbich, S. Dimmeler, Risk factors for coronary artery disease, circulating endothelial progenitor cells, and the role of HMG-CoA reductase inhibitors, Kidney Int. 67 (5) (2005) 1672–1676, https://doi.org/10.1111/j.1523-1755.2005.00261.x.
[49] K.S. Lau, et al., nNOS and eNOS modulate cGMP formation and vascular response in contracting fast-twitch skeletal muscle, Physiol. Genom. 2 (1) (2000) 21–27, https://doi.org/10.1152/physiolgenomics.2000.2.1.21.
[50] L. Xia, et al., Effect of nano-structured bioceramic surface on osteogenic differentiation of adipose derived stem cells, Biomaterials 35 (30) (2014) 8514–8527, https://doi.org/10.1016/j.biomaterials.2014.06.028.
[51] C. Yang, et al., 3D-Printed bioactive Ca3SiO5 bone cement scaffolds with nano surface structure for bone regeneration, ACS Appl. Mater. Interfaces 9 (7) (2017) 5757–5767, https://doi.org/10.1021/acsami.6b14297.
[52] K. Lin, et al., Tailoring the nanostructured surfaces of hydroxyapatite bioceramics to promote protein adsorption, osteoblast growth, and osteogenic differentiation, ACS Appl. Mater. Interfaces 5 (16) (2013) 8008–8017, https://doi.org/10.1021/am402089w.
[53] X. Wang, et al., Hypoxic tumor-derived exosomal miR-301a mediates M2 macrophage polarization via PTEN/PI3Kγ to promote pancreatic cancer metastasis, Cancer Res. 78 (16) (2018) 4586–4598, https://doi.org/10.1158/0008-5472.Can-17-3841.
[54] M.C. Runtsch, et al., Itaconate and itaconate derivatives target JAK1 to suppress alternative activation of macrophages, Cell Metabol. 34 (3) (2022) 487–501.e8, https://doi.org/10.1016/j.cmet.2022.02.002.
[55] L.B. Ivashkiv, L.T. Donlin, Regulation of type I interferon responses, Nat. Rev. Immunol. 14 (1) (2014) 36–49, https://doi.org/10.1038/nri3581.
[56] L. Arnold, et al., Inflammatory monocytes recruited after skeletal muscle injury switch into antiinflammatory macrophages to support myogenesis, J. Exp. Med. 204 (5) (2007) 1057–1069, https://doi.org/10.1084/jem.20070075.
[57] S.K. Wculek, et al., Oxidative phosphorylation selectively orchestrates tissue macrophage homeostasis, Immunity 56 (3) (2023) 516–530.e9, https://doi.org/10.1016/j.immuni.2023.01.011.
[58] S. Willenborg, et al., Mitochondrial metabolism coordinates stage-specific repair processes in macrophages during wound healing, Cell Metabol. 33 (12) (2021) 2398–2414.e9, https://doi.org/10.1016/j.cmet.2021.10.004.
[59] A.S. Rambold, E.L. Pearce, Mitochondrial dynamics at the interface of immune cell metabolism and function, Trends Immunol. 39 (1) (2018) 6–18, https://doi.org/10.1016/j.it.2017.08.006.
[60] M. Shi, et al., Europium-doped mesoporous silica nanosphere as an immune-modulating osteogenesis/angiogenesis agent, Biomaterials 144 (2017) 176–187, https://doi.org/10.1016/j.biomaterials.2017.08.027.
[61] Y. Feng, et al., A macrophage-activating, injectable hydrogel to sequester endogenous growth factors for in situ angiogenesis, Biomaterials 134 (2017) 128–142, https://doi.org/10.1016/j.biomaterials.2017.04.042.
[62] S.J. Hollister, Porous scaffold design for tissue engineering, Nat. Mater. 4 (7) (2005) 518–524, https://doi.org/10.1038/nmat1421.
[63] O.R. Mahon, et al., Nano-particle mediated M2 macrophage polarization enhances bone formation and MSC osteogenesis in an IL-10 dependent manner, Biomaterials 239 (2020) 119833, https://doi.org/10.1016/j.biomaterials.2020.119833.
[64] N.J. Horwood, Macrophage polarization and bone formation: a review, Clin. Rev. Allergy Immunol. 51 (1) (2016) 79–86, https://doi.org/10.1007/s12016-015-8519-2.
[65] Y. Jia, et al., Nanofiber arrangement regulates peripheral nerve regeneration through differential modulation of macrophage phenotypes, Acta Biomater. 83 (2019) 291–301, https://doi.org/10.1016/j.actbio.2018.10.040.
[66] X. Dong, et al., Aligned microfiber-induced macrophage polarization to guide schwann-cell-enabled peripheral nerve regeneration, Biomaterials 272 (2021) 120767, https://doi.org/10.1016/j.biomaterials.2021.120767.
[67] A.L. Cattin, et al., Macrophage-induced blood vessels guide schwann cell-mediated regeneration of peripheral nerves, Cell 162 (5) (2015) 1127–1139, https://doi.org/10.1016/j.cell.2015.07.021.
[68] A. Fantin, et al., Tissue macrophages act as cellular chaperones for vascular anastomosis downstream of VEGF-mediated endothelial tip cell induction, Blood 116 (5) (2010) 829–840, https://doi.org/10.1182/blood-2009-12-257832.